Physica Scripta

OPEN ACCESS

RECEIVED
21 November 2025

REVISED
26 December 2025

ACCEPTED FOR PUBLICATION
15 January 2026

PUBLISHED
28 January 2026

PAPER

Ramsauer-Townsend effect in Shannon and Fisher quantum information entropy, and the uncertainty principle in collision dynamics

Santanu Mondal* and **R Cabrera-Trujillo**

Instituto de Ciencias Fisicas, Universidad Nacional Autonoma de Mexico, Av. Universidad S/N, Col. Chamilpa, Cuernavaca, Morelos, 62210, Mexico

* Author to whom any correspondence should be addressed.

E-mail: sansantanu1991@gmail.com **and** trujillo@icf.unam.mx

Keywords: Ramsauer–Townsend effect, Shannon entropy, Fisher entropy, Heisenberg uncertainty principle, Crank-Nicolson technique

Abstract

In quantum physics, the scattering of a free particle by an impurity leads to the Ramsauer-Townsend effect, characterized by resonances in the cross section for transmission and reflection of the incident particle. In this work, we analyze this problem within the context of quantum information theory. In particular, we study the Shannon and Fisher entropy, as well as the Heisenberg uncertainty relations, to analyze the fragmentation of a wave packet in collision dynamics. As a primary contribution of this work, we note that these properties are directly related to each other through the same reflection and transmission coefficients as those of the Ramsauer-Townsend effect. Furthermore, we observe that the Heisenberg uncertainty principle satisfies the minimum value, i.e. $\hbar/2$, for the transmitted wave packet at resonance transmission and a maximum at higher fragmentation of the wave packet. We obtain that at resonance transmission, the reflected contribution to the uncertainty principle is zero with no violation of the Heisenberg principle. This leads, consequently, to the violation of it by the reflected wave packet, as there is no reflection. Moreover, the Shannon and Fisher quantum information entropy is found to be directly connected to Heisenberg's uncertainty principle for a dynamical system. Finally, we establish that these effects require the proper description of the time-dependent spreading of the wave packet to account for the proper dynamics.

1. Introduction

The scattering by a square well potential is a fundamental problem in quantum mechanics that explores how particles behave when encountering a region of space with an obstacle or impurity. A key aspect includes analyzing the scattering amplitude, which reveals information about the particle's interaction with the impurity. However, its treatments usually focus on the scattering of a time-independent plane wave, which exhibits phenomena such as reflection and transmission [1]. In this regard, the scattering of a time-dependent wave packet by a square potential (barrier or well) provides a unique opportunity to study some additional novel quantum phenomena, such as quantum tunneling times [2–6], the Hartman effect [7], and the transient interference effect on reflection and transmission [8].

One of the most intriguing quantum mechanical phenomena is the Ramsauer-Townsend (RT) effect [9, 10]. In 1921, this phenomenon was first observed in noble gases when low-energy electrons were scattered by atoms. Specifically, when a low-energy electron beam collides with certain atoms, such as xenon or argon, a minimal amount of scattering occurs. At some particular energies, the scattering cross section reaches a minimum because the electron, behaving as a wave, can partially or even completely transmit, depending on the nature of its wavelength and the characteristic properties of the impurity [11, 12]. This phenomenon can be well explained by a 1-D model of a plane wave that describes an electron scattered by a square-well potential. Such behavior of the system can be described through a straightforward solution of the time-independent

Schrödinger equation [1]. In this phenomenon, the RT effect is caused by constructive interference between the incoming and outgoing components of the wave function within the potential well or barrier, resulting in nearly complete transmission of the wave [1]. Experimentally, the RT effect can be directly probed in several systems, such as positron-argon collisions [13], xenon thyratrons [14], solid hydrogen [15], and ^{4}He–^{4}He scattering [16]. It also plays an important role in the study of fundamental quantum mechanical processes, including X-ray absorption fine structure in the zinc tetraimidazole clusters [17], as well as in theoretical frameworks such as quaternionic quantum mechanics [18] and q-deformed quantum mechanics [19–22]. It is worth noting that the use of the time-independent approach with plane waves inevitably leads to the loss of the time-resolved interference effects inherent in the full dynamical (time-dependent) treatment. Although time-dependent formulations explicitly describe the system's temporal evolution, neither framework is fundamentally superior. This correspondence closely parallels classical mechanics, where the Lagrangian formulation through Hamilton's principle remains fully equivalent to the step-by-step temporal evolution of Newtonian mechanics. However, only a few studies in the literature have explored this phenomenon when, instead of a plane wave, a Gaussian wave packet is used [23] (and references therein), mainly due to the complexity involved in solving analytically the time-dependent Schrödinger equation in this context.

Another important aspect of quantum mechanics is the study of *quantum information entropy* (QIE), which provides valuable information on the uncertainty and spatial distribution of quantum states [24]. In general, QIE serves as a measure of the localization or delocalization of the probability distribution associated with a quantum system. It is often quantified through various entropic measures, such as Shannon and Fisher information entropy, each offering unique perspectives on the system's behavior [25–28]. The Shannon entropy, regarded as a global measure of information entropy, reflects the degree of delocalization of the system. The Shannon entropy, $\mathcal{S}$, is defined as,

$$\mathcal{S} = -\int_{-\infty}^{\infty} \rho(x,\, t)\ln \rho(x,\, t)\, dx \tag{1}$$

where

$$\rho(x,\, t) = \Psi^{\dagger}(x,\, t)\Psi(x,\, t) \tag{2}$$

is the system probability density distribution as a function of position x and time t, and $\Psi(x, t)$ is the particle wave-function. A lower value of Shannon entropy typically corresponds to a more localized state, whereas a higher value indicates greater delocalization and spatial spreading of the wave function. Conversely, the Fisher entropy, known as a local measure of information entropy, behaves in a manner conjugate to the Shannon entropy in most of the quantum systems, being more sensitive to local variations in the probability distribution and is defined as

$$\mathcal{F} = \int_{-\infty}^{\infty} \frac{|\frac{d}{dx}\rho(x,\, t)|^2}{\rho(x,\, t)}\, dx. \tag{3}$$

Importantly, both of these entropic measures exhibit a close relationship with the ionization potential of quantum systems [29] and, as such, can be indirectly verified through experimental observations. A higher Shannon entropy indicates a more delocalized electron distribution, which can correlate with a lower ionization potential. Conversely, a higher Fisher entropy, which measures the sharpness of the probability density, often corresponds to a more localized electron distribution and a higher ionization potential. Such entropies have a wide range of applications, such as in quantum computing [24], chemical reactivity [30], correlation measure [31–37] and characterization of atoms and molecules [38–40]. Moreover, these entropic measures have proven to be highly effective as indicators of electron correlation and relativistic effects in confined atoms [41], in analyzing atomic orbital shape modifications [42], and in distinguishing virtual states in photon-induced transitions [43, 44]. Furthermore, extensive theoretical studies have been carried out on the time-independent treatment of atomic systems in different confinement scenarios, such as pressure confinement [45–49], plasma environments [50, 51], quantum dots [52–57], and fullerene cages [58]. In addition, Shannon entropy has also been established as an important tool for describing atomic collisions and molecular fragmentation [59]. However, to the best of our knowledge, no prior studies have explored the role of information entropy in the context of a scattering process within a real dynamical framework. In consequence, these entropies have significant potential for providing deeper insights into scattering processes.

Moreover, evaluating uncertainty in a quantum or classical measurement is equally crucial to understanding the fundamental limits of the system, in comparison to information entropy. However, unlike classical measurements, quantum measurements are inherently bound by a finite, irreducible minimum uncertainty [60, 61]. Heisenberg uncertainty, which is considered as the fundamental principle of quantum mechanics, precisely defines this intrinsic limit of uncertainty in quantum measurements. It is a variance-based measure of uncertainty between two conjugate observables, such as position, x, and momentum, p, associated with the corresponding operators $\hat{x}$ and $\hat{p}$, and is expressed in a product form as [60]

$$\Delta x\ \Delta p \geqslant \frac{\hbar}{2}. \tag{4}$$

The Heisenberg uncertainty principle has profound implications not only in information theory but also across a wide range of fundamental research areas, including quantum entanglement detection [62–64], quantum non-cloning [65, 66], quantum cryptography [67], quantum synchronization [68, 69], quantum metrology [70], and the detection of mixedness [71, 72], among others. Importantly, under the influence of external perturbations or under extreme confinement conditions, the Heisenberg uncertainty principle for a real atom exhibits intricate behavior, yet it invariably adheres to its fundamental lower bound [73] (and references there in). However, the same problem has not yet been explored for a wave packet fragmentation in a collision.

In the present work, as a first approach towards this study, we revisit the reflection and transmission concepts by modeling the incoming particle as consisting of a Gaussian wave packet scattered by a square well with fixed width and depth. The reason for this is that we are interested in wave packet's dynamics where equation (1) and (3) can provide physical information on the fragmentation dynamics. Goldberg *et al* [23] reported a detailed description of the time-dependent evolution for a Gaussian wave packet, using computer-generated motion pictures to illustrate the phenomena of reflection and transmission from a square well or barrier potential. However, the reflection and transmission coefficients depend on the energy of the incident particle as well as on the width and height (or depth) of the potential, making this problem analytically intractable. The square well potential is well justified since it has been used to model interactions between nucleons (protons and neutrons) within the nucleus in nuclear physics [74]. As mentioned above, it is also used to study the scattering of electrons by noble gas atoms, where a minimum in the scattering cross-section is observed at certain energies [9, 10]. Furthermore, this model is used to determine the scattering length and effective range, which are important parameters in low-energy scattering, characterizing the interaction at long distances [75]. Some other works on the study of the infinite square well and delta potential are available in the literature [76, 77]. In this work, the corresponding time-dependent one-dimensional Schrödinger equation is solved numerically using the finite-differences method, with the time evolution handled by the Crank-Nicolson technique [78]. However, it should be mentioned that the full three-dimensional treatment of the RT-effect is more realistic, but a one-dimensional model can often approximate the energy dependence and show the qualitative behavior of the cross-section through the reflection and transmission coefficients. While not fully realistic, one-dimensional models can still provide physical insight into how the scattering process works and why the RT-effect occurs. For instance, it can give an understanding of how the electron's wave function interacts with the potential, how energy quantization affects the scattering, and how interference can result in the observed cross-section minimum. The one-dimensional model is, of course, an approximation. In reality, the interaction between the electron and the target is fully three-dimensional, with the electron scattering in all directions, and the quantum wave function is spread out in three-dimensional space. However, for first-order approximations or for conceptual models, one-dimensional simplifications are often acceptable and can provide the core understanding without the need for overly complex calculations. Thus, the present work is a benchmark towards the three-dimensional goal. Therefore, the reflected, transmitted, and trapped portions of the wave packet estimated from the Crank-Nicolson technique are then used to calculate the respective scattering coefficients. We verify the Ramsauer-Townsend effect by systematically varying the incident particle energy. Additionally, we compute the Shannon and Fisher entropies and analyze their behavior as functions of the incident particle energy. Importantly, the calculation of entropic measures offers an advantage over macroscopic (global) quantities, such as scattering coefficients, by providing microscopic or structural insights into the complexity, delocalization, and coherence of the wavefunction. Thus, the time evolution of both the scattering coefficients (macroscopic) and the information entropic (microscopic) quantities is examined in detail to gain the overall understanding of the dynamical process. Furthermore, we investigate how the scattering quantum process correlates with the uncertainty principle and QIE.

The structure of the work is organized as follows: in section 2, we provide a brief overview of the theory, as well as the analytical and numerical techniques employed. In section 3, we present a thorough discussion of our findings. Finally, in section 4, we conclude with a summary of our work. Throughout this work, all parameters are expressed in atomic units unless stated otherwise.

2. Theory

2.1. Scattering by a square well potential

The time-dependent Schrödinger equation for a particle described by the wave-function $\Psi(x, t)$ is

$$-\frac{1}{2m}\frac{\partial^2\Psi}{\partial x^2} + V(x)\Psi = i\frac{\partial\Psi}{\partial t}, \tag{5}$$

where m is the particle's mass. The square well potential $V(x)$ is given by

$$V(x) = \begin{cases} V_0 & \text{for} \quad |x| \leqslant R_0 \\ 0 & \text{elsewhere}. \end{cases} \tag{6}$$

The parameters R_0 and V_0 refer to the width and depth (or height for a potential barrier) of the potential. In this work, we shall consider the case of an attractive well.

The scattering solutions for collision energy $E > 0$ are reported in Quantum Mechanics textbooks [1, 79]. For the case of an incident particle from the left, $x < -R_0$, we have

$$\psi(x) = Ae^{ik_I x} + Be^{-ik_I x}, \tag{7}$$

where $k_I = \sqrt{2\,mE} = mv$, corresponding to the incident projectile momentum. Inside the well, where $V(x) = -V_0$,

$$\psi(x) = C\sin(k_{II}x) + D\cos(k_{II}x), \tag{8}$$

for $-R_0 < x < R_0$, with, $k_{II} = \sqrt{2\,m(E + V_0)}$. To the right, assuming that there is no incoming particle from the right, we have

$$\psi(x) = Ge^{ik_I x}, \tag{9}$$

for $x > R_0$. Here, A is the incident amplitude, B is the reflected amplitude, and G is the transmitted amplitude. From the continuity of the wave function at $x = -R_0$ and $x = R_0$, one can determine the probability amplitudes. In particular, the transmitted and reflected probabilities are given by [1, 79]

$$T = \left|\frac{A}{G}\right|^2 = \frac{1}{1 + \frac{1}{4\epsilon(1+\epsilon)}\sin^2\left(\sqrt{8\beta(1+\epsilon)}\right)}, \tag{10}$$

with the condition that $R + T = 1$. The reduced energy ϵ and β are given by $\epsilon = E/V_0$ and $\beta = mR_0^2V_0$. Resonance transmission occurs when $\sqrt{8\beta(1+\epsilon)} = n\pi$, with $n = 1, 2, 3, \ldots$, such that

$$\epsilon + 1 = \frac{\pi^2 n^2}{8\beta}. \tag{11}$$

This can be rewritten as

$$E_n + V_0 = \frac{\pi^2}{2m(2R_0)^2}n^2, \tag{12}$$

which happens to be precisely the allowed energies for the infinite square well, shifted from the bottom of the square well. This resonance transmission is the Ramsauer-Townsend effect, which occurs when the target becomes completely invisible to the projectile. From equation (8), we see then that $k_{II} = mv_{II} = \pi n/2R_0$, such that the de Broglie wave length of the particle inside the well must be an integer fraction of the well width, i.e. $\lambda_{II} = 4R_0/n$.

With respect to the wave function, as seen from equation (7), it is not normalizable as it is completely delocalized in the configuration space, such that one can not say anything about density and entropy. The dynamics of a free particle, described by a Gaussian wave packet, becomes a better choice since it is a superposition of plane waves with a distribution of momenta centered around a mean value. The width of the wave packet represents the uncertainty in the position of the particle, which spreads over time as it propagates. This spreading is a consequence of the wave-particle duality and leads to the Heisenberg uncertainty principle. The time evolution of a free Gaussian wave packet is given by [79]

$$\psi_g(x,\,t) = \left(\frac{2}{\pi\omega^2(t)}\right)^{1/4} e^{-\frac{(x-x_g(t))^2}{\omega^2(t)} + ikx} \tag{13}$$

where $\omega(t) = \omega_0\sqrt{1 + 2it/m\omega_0}$ is the width of the Gaussian wave packet, $x_g(t)$ is the position at time t, ω_0 its initial width and $E = (k^2 + 1/\omega^2)/2m$. However, as mentioned earlier, the analytical solution for the reflection or transmission of a free particle, represented by a Gaussian wave packet when colliding with a square-well potential, has not been reported yet to the author's knowledge. Thus, in order to solve equation (5), we resort to a numerical time-dependent propagation through the Crank-Nicolson approach to obtain the scattering dynamics within a finite-differences approach [78, 80, 81]. A brief discussion on this is given below. Before that, let us make an analysis on the consequences of using this analytical wave function.

2.2. Shannon entropy, Fisher entropy, and Uncertainty principle for a Gaussian wave-packet

By comparing equation (13) to equation (7), and supported by the numerical results shown in section 3 (see below), we construct, at the end of the collision, the wave function on the left of the square as a reflected Gaussian wave packet

$$\psi(x) = \sqrt{R}\,\psi_r(x) \tag{14}$$

and the transmitted wave function as

$$\psi(x) = \sqrt{T}\,\psi_t(x), \tag{15}$$

where R and T are the RT coefficients, given by equation (10). Here, considering the scattering coefficients to represent a proper definition of reflected and transmitted Gaussian wave packet is physically correct. A plane wave provides an idealized representation of a free particle and is therefore well-suited for determining the scattering coefficients R and T, which characterize the interaction with the potential. These coefficients are intrinsic properties of the scattering potential and depend only on the particle energy (or momentum). In the present work, however, we employ a Gaussian wave packet with a sufficiently large spatial width so that it closely resembles a free particle wave packet over the interaction region. Such a broad Gaussian packet is effectively quasi-monochromatic and can be viewed as a superposition of plane waves narrowly distributed around a central momentum. Under this condition, each plane-wave component experiences nearly identical scattering, allowing the plane-wave coefficients R and T to accurately describe the reflected and transmitted portions of the Gaussian wave packet. This choice combines physical transparency with numerical practicality, while preserving the essential scattering physics. Here, ψ_r is the reflected Gaussian wave packet at position $x_r(t)$, while ψ_t is at position $x_t(t)$ for the transmitted Gaussian wave packet. With this, our plane wave is now normalizable and one can determine Shannon, Fisher, and Heisenberg uncertainty relations. By employing equation (2), from equations (14) and (15), it can be found that

$$\rho(x,\,t) = R|\psi_r|^2 + T|\psi_t|^2 + 2\sqrt{RT}\,\Re[\psi_r^\star\psi_t] \tag{16}$$

Since in the asymptotic limit after scattering, both the reflected and transmitted wave packet are non-overlapping in space i.e., $\psi_r^\star\psi_t \approx 0$. This gives,

$$\rho(x,\,t) \approx R|\psi_r|^2 + T|\psi_t|^2 = R\rho_r(x,\,t) + T\rho_t(x,\,t) \tag{17}$$

Now, with the help of equation (1), one finds

$$\mathcal{S}_T = -\int [R\rho_r(x,\,t) + T\rho_t(x,\,t)]\ln[R\rho_r(x,\,t) + T\rho_t(x,\,t)]\,dx \tag{18}$$

With a little bit of algebra, one obtains

$$\mathcal{S}_T = S_r + S_t \tag{19}$$

where S_i is given by

$$S_i = C_i\mathcal{S}_i - C_i\ln C_i. \tag{20}$$

Here, C_i denotes either R or T, with i corresponding to either r or t. The entropies S_r and S_t quantify the information content carried by the reflected and transmitted parts of the wave packet, respectively. However, these do not represent the *true* Shannon entropies of the reflected and transmitted wave packets. We employ the term *true* to emphasize that Shannon entropy must be derived from the corresponding normalized density distributions, which is not the case for S_r and S_t. The *true* Shannon entropy $\mathcal{S}_i$ is given by the same equation (1) with the density calculated with the Gaussian ψ_i, such that

$$\mathcal{S}_i = \frac{1}{2}\left[1 - \ln\left(\frac{2}{\pi\omega^2}\right)\right], \tag{21}$$

is the contribution from the normalized reflected and transmitted part of the Gaussian wave packet. For this result, we have assumed that there is no overlap between the reflected and transmitted Gaussian wave packets.

For the total Fisher entropy, equation (3), gives

$$\mathcal{F}_T = F_r + F_t = R\mathcal{F}_r + T\mathcal{F}_t \tag{22}$$

where the true Fisher entropy $\mathcal{F}_i$ is given by the same equation (3) for the Gaussian contribution ψ_i, such that

$$\mathcal{F}_i = \frac{4}{\omega^2}. \tag{23}$$

Since $R + T = 1$, then

$$\mathcal{F}_T = \frac{4}{\omega^2}. \tag{24}$$

Thus, the total Fisher entropy is the same as the Fisher entropy of the reflected or transmitted contribution. These expressions are independent of the position of the reflected wave packet but depend on time through the time-dependent width.

With respect to the uncertainty principle, we obtain the following expectation values for position

$$\begin{aligned}\langle x\rangle &= R\langle x\rangle_r + T\langle x\rangle_t,\\ \langle x^2\rangle &= R\langle x^2\rangle_r + T\langle x^2\rangle_t.\end{aligned} \tag{25}$$

For the case of the Gaussian wave packet, we get

$$\begin{aligned}\langle x\rangle_r &= x_r\\ \langle x^2\rangle_r &= \left[\frac{\omega^2}{4} + x_r^2\right],\end{aligned} \tag{26}$$

with equivalent equations for the transmitted part.

For the momentum, one obtains

$$\begin{aligned}\langle p\rangle &= R\langle p\rangle_r + T\langle p\rangle_t,\\ \langle p^2\rangle &= R\langle p^2\rangle_r + T\langle p^2\rangle_t\end{aligned} \tag{27}$$

where

$$\begin{aligned}\langle p\rangle_r &= k\\ \langle p^2\rangle_r &= \left[k^2 + \frac{1}{\omega^2}\right].\end{aligned} \tag{28}$$

Then, the variances of position and momentum are given by

$$\begin{aligned}(\Delta x_T)^2 &= (\Delta x_r)^2 + (\Delta x_t)^2 - 2RT\langle x\rangle_r\langle x\rangle_t\\ (\Delta p_T)^2 &= (\Delta p_r)^2 + (\Delta p_t)^2 - 2RT\langle p\rangle_r\langle p\rangle_t\end{aligned} \tag{29}$$

with

$$(\Delta A_i)^2 = C_i\langle A^2\rangle_i - C_i^2\langle A\rangle_i^2. \tag{30}$$

and A_i is either x or p and again, C_i is either R or T with i being either r or t or the total, respectively.

For the Gaussian wave packet, one obtains

$$\begin{aligned}\Delta x_r &= \sqrt{\frac{R\omega^2}{4} + x_r^2(R - R^2)},\\ \Delta p_r &= \sqrt{\frac{R}{\omega^2} + k^2(R - R^2)}.\end{aligned} \tag{31}$$

Consequently, Heisenberg's uncertainty principle, for the reflected contribution, is

$$\Delta x_r\Delta p_r = \frac{R}{2}\sqrt{1 + T\left(\frac{4x_r^2}{\omega^2} + \omega^2k^2\right) + (2x_rkT)^2}. \tag{32}$$

Equivalent equations for the transmitted part are obtained by swapping R and T as well as the sub-indices r and t in these previous equations. Note here that ω and x_r are functions of time. From equation (31), we find that the variance is correlated through the reflection and transmission wave packets and it is not just the sum.

2.3. Scaling to an effective mass

By making the following change of variable $x' = x/R_0$ and $\epsilon = E/V_0$ in equation (5), the time-independent Schrödinger equation reduces to

$$-\frac{1}{2\beta}\frac{\partial^2\psi}{\partial x'^2} + V'(x')\psi = \epsilon\psi(x'). \tag{33}$$

where $\psi = \psi/\sqrt{R_0}$ to maintain the normalization condition. With this, the potential is given by

$$V'(x') = \begin{cases}-1 & \text{for} \quad |x'| \leqslant 1\\ 0 & \text{elsewhere}.\end{cases} \tag{34}$$

Thus, equation (33) provides the bound and continuum solutions for a particle of effective mass $\beta = mR_0V_0^2$ in a square well potential of unit area. This has the advantage that we do not need to carry out the dynamics for all combinations of the square well parameters R_0 and V_0. Thus, square wells with the same $\beta = mR_0V_0^2$ show the same universal behavior. This scaling becomes convenient when performing the numerical analysis, as seen in the following.

Regarding QIE, with this scaling, equation (1) for the Shannon entropy becomes

$$\mathcal{S} \to S + \ln R_0 \tag{35}$$

and the Fisher entropy reduces to

$$\mathcal{F} \to \frac{F}{R_0^2}, \tag{36}$$

but now S and F evaluated with the density in the scaled coordinates, i.e. $\rho = |\psi(x',\ t)|^2$ and it being a function of β.

Regarding the uncertainty relations, we have that

$$\begin{aligned} \Delta x &= R_0 \Delta x', \\ \Delta p &= \frac{\Delta p'}{R_0}, \end{aligned} \tag{37}$$

such that $\Delta x \Delta p = \Delta x' \Delta p'$, i.e. the uncertainty principle is independent of the scaling. Furthermore, the wider the well, the larger the variance in x, while the smaller the uncertainty in the momentum.

Therefore, the scaling highlights that the impurity size plays an important role in QIE and uncertainty measurements, and the scaling allows the extraction of this as a universal feature [82, 83]. With this, the results of equations (21) to (32) are obtained systematically under the integrals of equations (35) and (36), simply replacing the variables with those in the scaled system. In what follows, we will work in the scaled coordinates and drop the primes.

2.4. Finite-differences approach

Let us define the Hamiltonian of the system as $\hat{H} = \hat{T} + \hat{V}$, where $\hat{T} = -\frac{1}{2\beta}\frac{\partial^2}{\partial x^2}$ and $\hat{V}$ are the kinetic energy and potential energy operators, respectively. The general solution to equation (33) is given by

$$\psi(x,\ t + \Delta t) = \hat{U}(t,\ t + \Delta t)\psi(x,\ t), \tag{38}$$

where the time evolution operator is given by $\hat{U}(t,\ t + \Delta t) = e^{-i\hat{H}\Delta t}$. Therefore, equation (38) can be recast as,

$$\psi(x,\ t + \Delta t) = e^{-i\hat{H}\Delta t}\psi(x,\ t) = e^{-i(\hat{T}+\hat{V})\Delta t}\psi(x,\ t).$$

By using the '*split operator*' technique [80], one reduces the time-propagation to matrix algebra for each time step. By defining $f(x,\ t) = e^{-i\hat{V}\Delta t}\psi(x,\ t)$, discretizing the wave function in a numerical mesh such that $\psi(x,\ t) \to \psi(x_k,\ t^n) \to \psi_k^n$ where $x \to x_k$ and $t \to t^n$, one recasts the problem as

$$\mathbf{M}^{+}\psi^{n+1} = \mathbf{M}^{-}f^n = \mathbf{b}, \tag{39}$$

where ψ^{n+1} is an array with elements ψ_k^{n+1} with $k = 1, 2, \ldots, N$ and N is the number of points in the mesh. The matrix elements of the tri-diagonal matrix $\mathbf{M}^{\pm}$ are $M_{i,i}^{\pm} = 1 \pm 2\nu$, $M_{i,i+1}^{\pm} = M_{i,i-1}^{\pm} = \mp 2\nu$, where $\nu = \frac{i\Delta t}{4\beta(\Delta x)^2}$. Here Δt and Δx are the time and space grid steps in a uniform mesh. We have solved the above equation numerically using our own developed FORTRAN code. Specifically, the subroutines ZGTTRF and ZGTTRS from the LAPACK and BLAS libraries were employed to efficiently solve the resulting matrix equation.

2.5. Numerical implementation

At first, we consider a square well potential as the one given by equation (34), where by choosing different values of β one obtains the dynamics for all V_0 and R_0, which are constrained to that β. In this work, we select the values of $\beta = 5, 25$, and 100. The spatial domain, in the scaled coordinates, is chosen as $x \in [-200, 200]$, divided into $N = 20,000$ mesh points. This results in a spatial step size of $\Delta x = 0.02$ a.u. The time step is set to $\Delta t = 0.001$ a.u. to ensure numerical convergence. The initial position of the incident wave packet is placed at a sufficiently large distance $x_0 = -40$ with respect to the square well in the scaled coordinated. The initial width of the wave packet, ω_0, in the scaled domain, is set at 15, so that the wave packet is wide enough to represent a plane wave. The values of ϵ were chosen from 0.01 to 10 in a logarithmic mesh that provided 100 energy values.

3. Results and discussions

3.1. Reflection and transmission density

By solving equation (39), the scattered wave function is obtained for each time step, which is subsequently used to determine the density distribution. As mentioned before, from here on, we use the scaled units and show the

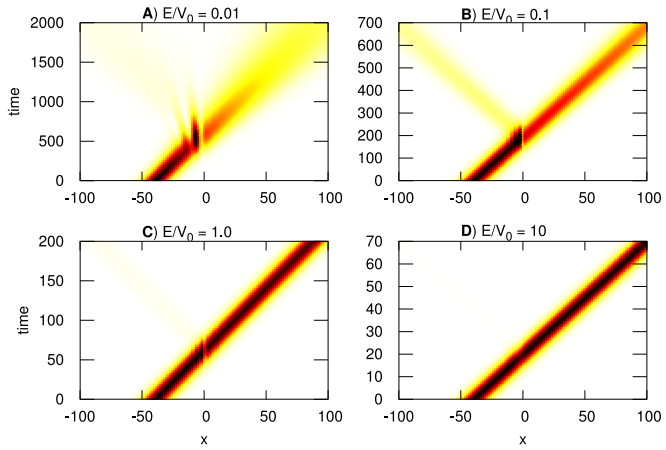

Figure 1. The probability density distribution of the scattered wave $\rho(x, t)$ as a function of position x for different time t for the case of $\beta = 5$. In (**A**), we show the case for incident particle energy of $\epsilon = 0.01$, in (**B**), for $\epsilon = 0.1$, in (**C**), for $\epsilon = 1$, and in (**D**), for $\epsilon = 10$. See text for discussion.

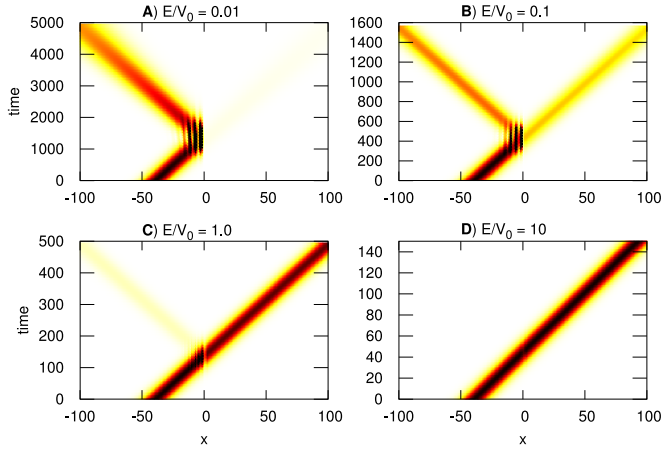

Figure 2. The same as figure 1, but for the case of $\beta = 25$.

results without the prime variable, for simplicity. In figure 1, we show the probability density evolution as a function of x and t for four different collision energies, $\epsilon = 0.01$, 0.1, 1, and 10. In figure 1(A), we show the case for $\beta = mV_0R_0^2 = 5$. Our results reveal that for low collision energy, as the Gaussian wave packet approaches the potential well, the density shows interference near the origin due to the collision with the well. As the wave packet passes through, the distribution splits into two distinct components—reflected and transmitted waves. However, this splitting behavior depends explicitly on both ϵ and β. To clarify this, let us first concentrate on figure 1(A), for $\epsilon = 0.01$. It is observed that, despite the low-energy collision ($E \ll V_0$), the Gaussian wave packet undergoes a near complete transmission through the potential well following an initial disturbance at the well position. This can be explained from equation (11), since for $\epsilon = 0.01$, we find that the resonance occurs for $n = 2$, i.e., it satisfies a near-resonance condition. Under such circumstances, constructive interference inside the well enhances the probability of transmission, making it dominant over reflection. On the other hand, as ϵ increases and depending on the resonance condition, destructive interference may occur within the well. This leads to partial reflection of the wave packet, as evident in figure 1(B) and (C). In figure 1(B), we find that $n = 2.1$ for $\epsilon = 0.1$ and in **C** $n = 2.85$ for $\epsilon = 1$. Thus, the case **B** shows a slight reflection, while **C** shows almost a full transmission. Interestingly, the case shown in **C** for $\epsilon = 1$ corresponds to the condition $E = V_0$, which still shows some reflection. In contrast, at high energy, such as $\epsilon = 10$ where $E \gg V_0$, the wave packet is only weakly affected by the potential depth. Consequently, it is almost entirely transmitted, with only a faint reflected contribution, as observed in figure 1(D). Also, note that as $\epsilon = E/V_0$ increases, the time of the dynamics is reduced, as observed in figure 1.

In contrast, the case for $\beta = 25$ is illustrated in figure 2. For low collision energy, as shown in figure 2(A) for $\epsilon = 0.01$, the post-collision density is predominantly contributed by the reflected part of the wave packet. For this case, equation (11) gives $n = 4.2$ out of resonance. For the case of figure 2(B), we obtain $n = 4.72$ for $\epsilon = 0.1$,

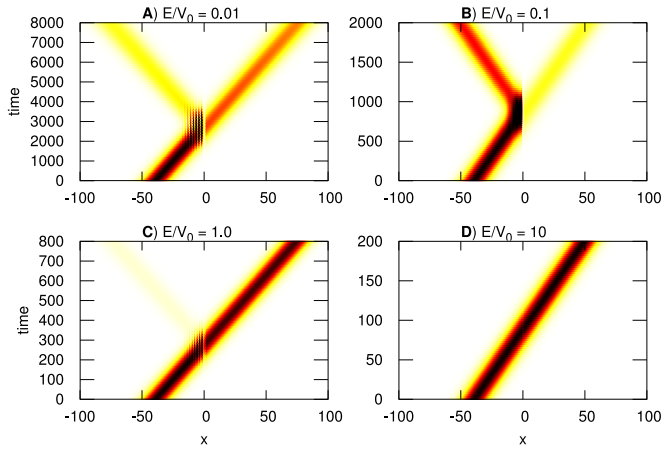

Figure 3. The same as figure 1, but for the case of $\beta = 100$.

while for figure 2(C), we obtain $n = 6.37$ for $\epsilon = 1$, out of resonance, while for figure 2(D) one has almost full transmission due to the high energy collision for $\epsilon = 10$.

Finally, for the case $\beta = 100$, shown in figure 3, the dominant contribution at energy $\epsilon = 0.01$ arises from the transmitted wave packet with resonance with the level $n = 9$ as observed in figure 3(A). For the case of $\epsilon = 0.1$ is shown in figure 3(B), resulting in $n = 9.44$, showing reflection, as well as for the case of figure 3(C), where $n = 12.7$ for $\epsilon = 1$. However, in all the results at high energy ($\epsilon = 10$), almost complete transmission is observed, which appears to be independent of the value of β. These intricate behaviors are better understood through the calculation of the scattering coefficients, as discussed in the following section.

3.1.1. Reflection and transmission coefficients: Ramsauer-Townsend effect

Next, using the density distribution $\rho(x, t)$ of the wave packet, we determine the scattering coefficients corresponding to the reflected, R, transmitted, T, and transient trapped, T_{tr}, components as,

$$\begin{aligned} R &= \int_{-\infty}^{-a} \rho(x,\, t)\, dx \\ T &= \int_{-a}^{\infty} \rho(x,\, t)\, dx \\ T_{tr} &= \int_{-a}^{a} \rho(x,\, t)\, dx. \end{aligned} \tag{40}$$

The value of $a = 3$ is used in order to consider the tail of the possible trapped particle in the well [79].

In figure 4, we present R and T from the numerical calculations (symbols). The analytic results, from equation (10), are overlaid in figure 4, where the red solid line and blue dashed lines represent R and T, respectively. As is evident, the numerical data closely match the analytical results. The RT effect is effectively explained by treating the incident wave as a plane wave modulated by a Gaussian wave packet. The oscillatory nature arises due to the destructive interference between the reflected wave from the well at $x = \pm 1$ and the corresponding resonance condition. Upon a closer examination of all three panels of this figure, the following preliminary observations can be drawn: (*i*) At very low energy ($\epsilon \to 0$), the transmission coefficient T dominates over the reflection coefficient R for $\beta = 5$, whereas the opposite behavior is observed for $\beta = 100$. (*ii*) The number of half oscillations in both R and T increases with increasing β. (*iii*) For $\beta = 5$, the variations of R and T remain well separated and do not intersect. In contrast, for $\beta = 25$, a single crossing point is observed, and this number increases to two for $\beta = 100$. At each crossing, the values satisfy $R = T = 0.5$. (*iv*) For $\beta = 25$, the crossing between R and T occurs near $\epsilon \approx 0.1$, while for $\beta = 100$, the two crossings occur approximately at $\epsilon \approx 0.02$ and $\epsilon \approx 0.15$. The first observation can be well explained by studying the quasi-bound resonances that satisfy the condition given in equation (11), i.e.

$$\epsilon_n = \frac{n^2\pi^2}{8\beta} - 1. \tag{41}$$

It can be found that for $\beta = 5$, there exist only two bound states for the stationary equation (33), i.e. $\epsilon_1 = -0.75326$ and $\epsilon_2 = -0.013$. Due to $\epsilon_2 \to 0$, the resonant wave packet tends to overlap with the low-energy wave packets. This can exhibit quasi-resonances near $\epsilon \to 0$, resulting in the enhancement in the transmission coefficient. Additionally, at low energy $\epsilon \to 0$, $k_I \to 0$ and $\lambda_I \to \infty$. This makes the wave packet outside the well almost unperturbed, which also favors the dominant transmission. On the other hand, for $\beta = 25$, four bound

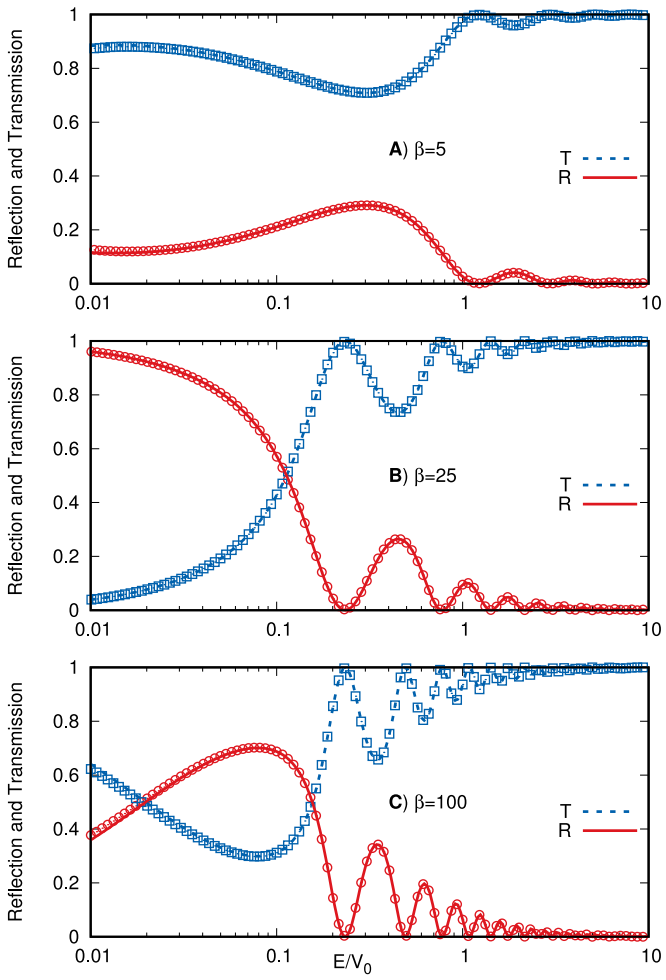

Figure 4. Reflection, R, (red solid line) and transmission, T, coefficients (blue dashed line) as a function of the ratio of $\epsilon = E/V_0$. In **A**, we show the case $\beta = 5$, in **B**, we show the case $\beta = 25$, and in **C**, the case $\beta = 100$ is shown. The same color symbols refers to the numerical results obtained for R and T with the initial Gaussian wave packet. See text for discussion.

states are formed with energies $\epsilon_1 = -0.95065$, $\epsilon_2 = -0.80261$, $\epsilon_3 = -0.55587$, and $\epsilon_4 = -0.21043$. Notably, the last bound state energy ϵ_4 lies significantly below the continuum threshold, indicating that no quasi-resonance features emerge in the low-energy regime ($\epsilon \to 0$) and consequently the coefficient R dominates over T. However, for $\beta = 100$, a total of nine bound states can be found. Intricately, the bound state ϵ_9 has the energy -0.0007, which again supports the quasi-resonance condition. Therefore, for the low-energy regime, again T dominates over the coefficient R. It is worth mentioning here that such an oscillatory behavior of R and T was first reported by Ramsauer and Townsend, and they coined it as '*resonant transmission*' [9, 10]. Next, the number of oscillations (case (*ii*)) in T (or R), as also depicted in figure 4, can be exactly estimated with the help of equation (10). For this, we have to count the number of resonances at which $T = 1$ for the energy range $\epsilon \in [0.01, 10]$. Then equation (41) is used to determine the maximum number of complete half oscillations $n_{\max}$. The nodes of such oscillation provide the exact positions of the resonances. Thus, the maximum number of complete half oscillations is evaluated as,

$$n_{\max} = \sqrt{\frac{8\beta(1 + \epsilon_{\max})}{\pi^2}}. \tag{42}$$

Evidently, since the upper bound of the energy is fixed at $\epsilon_{\max} = 10$, the maximum number of half oscillations $n_{\max}$ is governed solely by the effective mass β. This behavior indicates that $n_{\max}$ scales proportionally with the square root of the effective mass, i.e., $n_{\max} \propto \sqrt{\beta}$. Finally, the values of $n_{\max}$ for $\beta = 5$, 25, and 100 are respectively found to be 6, 14, and 29. This indicates that increasing β allows a greater number of resonant states to form. The explanation for the observations (*iii* and *iv*) is quite straightforward and it can be understood by recalling equation (10). Evidently, at the point of intersection $R = T = \frac{1}{2}$. This gives,

$$\sin^2\left(\sqrt{8\beta(1 + \epsilon)}\right) = 4\epsilon(1 + \epsilon). \tag{43}$$

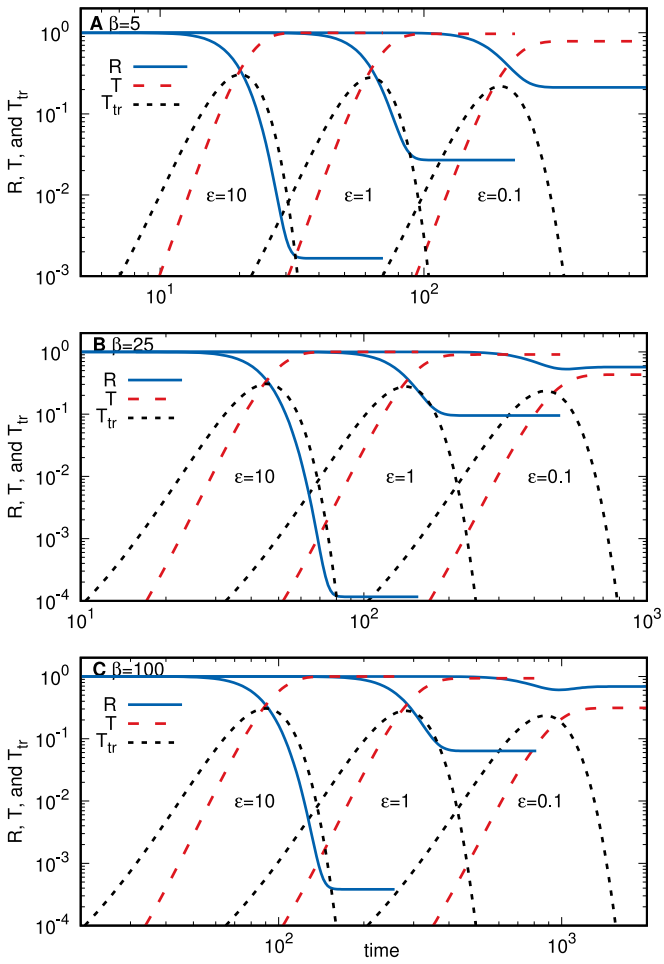

Figure 5. Time evolution of the scattering coefficient R (blue solid line), T (red dashed line) and T_{tr} (black dotted line) for the case of three different energies $\epsilon = 0.1$, 1 and 10. In **A**, we show the case $\beta = 5$, in **B**, the case $\beta = 25$, and in **C**, the case $\beta = 100$. See text for discussion.

By solving this equation for $\beta = 5$, no accessible roots are found. In contrast, for $\beta = 25$, a single accessible root occurs at $\epsilon \approx 0.113$. On the other hand, when $\beta = 100$, two accessible roots emerge at $\epsilon \approx 0.019$ and $\epsilon \approx 0.155$. The condition of $R = T = \frac{1}{2}$ indicates that the Gaussian wave packet has equal probabilities of being transmitted and reflected, which are controlled solely by two parameters β and ϵ. But more importantly, no trapping occurs. Physically, this refers to a point of balanced interference, i.e., neither fully constructive nor fully destructive. This scenario is closely associated with the first resonance of the square well.

The time evolution of the reflection, R, transmission, T, and transient trapped, T_{tr}, components is illustrated in figure 5 for three different incident energies: $\epsilon = 0.1$, 1, and 10, as well as for the three cases of $\beta = 5$, 25, and 100. The overall behavior of R, T and T_{tr} remains qualitatively similar for all β values considered, as discussed below. It is observed that the low-energy particle ($\epsilon = 0.1$ a.u.) takes a longer time to reach the potential well due to its lower collision energy. During its interaction with the well, a non-zero transient component, T_{tr} is observed, and it exhibits a Gaussian-like profile. As the energy increases, the peak of this profile increases monotonically, while its width becomes narrower, indicating a reduced trapping duration. The transmittance, T, for particles at all energy levels initially remains zero but increases in a step-like manner as time progresses. After the collision with the potential well, T eventually converges to a particular value for low collisional energy. As the collisional energy increases, the final value of T also increases, reaching $T \to 1$ for the high-energy case, $\epsilon = 10$, indicating complete transmission. An opposite trend is observed for the reflection coefficient, R, which decreases with increasing energy. This behavior signifies that at high energies, the particle possesses sufficient kinetic energy for the potential well to act effectively as a transparent medium, that is, to overcome the well or barrier.

3.1.2. Shannon and Fisher entropy

Information entropy, such as Shannon and Fisher entropy, provides an excellent opportunity to underscore the overall deformation of the density distribution due to the collision of the particle with the square well, in

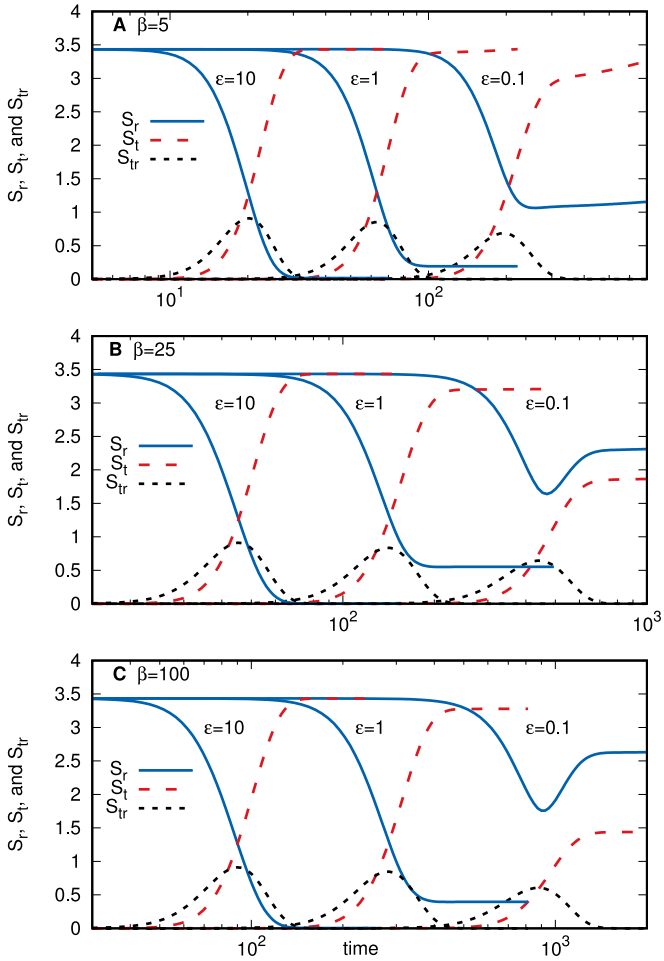

Figure 6. Time evolution of Shannon entropy $S_i \equiv \mathcal{S}_i - \ln R_0$ (i refers to r or t or tr), from equation (35). Here, the reflected, S_r, is shown with solid blue line, the transmitted, S_t, with red dashed line, and the transient trapped, S_{tr} with black short-dashed line. The case $\beta = 5$ is shown in **A**, $\beta = 25$ in **B**, while $\beta = 100$ is shown in **C**. See text for discussion.

particular when there is fragmentation in the system. For the case of the FD numerical calculations, motivated by the results of figures 1–3, we find that the final wave function can be split as

$$\psi(x,\, t) = \psi_r(x,\, t) + \psi_t(x,\, t) \tag{44}$$

with ψ_r corresponding to the reflected wave packet for $x < -R_0$ and ψ_t the transmitted wave packet for $x > R_0$, with no overlap between these two functions. By normalizing these two contributions, we have that

$$\psi(x,\, t) = \sqrt{R}\,\tilde{\psi}_r + \sqrt{T}\,\tilde{\psi}_t \tag{45}$$

where $\tilde{\psi}_i = \psi_i/\sqrt{C_i}$. Notice here that $\tilde{\psi}$ is the numerical wave function and not the Gaussian approximation used in equations (14) and (15). With this expression, the determination of expected values, numerically, is readily carried out. Interestingly, with the definition of equation (44), the total Shannon entropy reduces to an equation equivalent to equation (19).

In the following, we focus on the variation of the Shannon entropy in the scaled coordinates for both the reflected and transmitted waves. In particular, we examine reflected S_r, transmitted S_t and trapped component S_{tr} of the Shannon entropy, in the scaled coordinates, which are exactly equivalent to $S_r - \ln R_0$, $S_t - \ln R_0$, and $S_{tr} - \ln R_0$ as functions of ϵ in the physical system. Before delving into a detailed discussion of the entropic measures, it is essential to understand the explicit time dependence of the wave packet. As established in the earlier discussion, the wave packet undergoes increasing dispersion as it evolves over time. Consequently, the components of Shannon entropy also exhibit a time-dependent behavior [see equation (21)]. To illustrate this, the time evolution of the S_t, S_r and S_{tr} for three different values of $\beta = 5$, 25 and 100 is presented in figure 6. A closer examination of all three cases reveals two distinct characteristics. First, for a given ϵ, both S_t and S_r remain constant for a certain period of time, attaining a maximum value for the transmitted wave packet and a minimum for the reflected component. Eventually, the entropy stabilizes again, with the reflected part exhibiting the minimum value and the transmitted part reaching the maximum. Second, due to the collision energy, ϵ, the time required for the Shannon entropy to converge differs significantly for different ϵ, the lower the ϵ, the

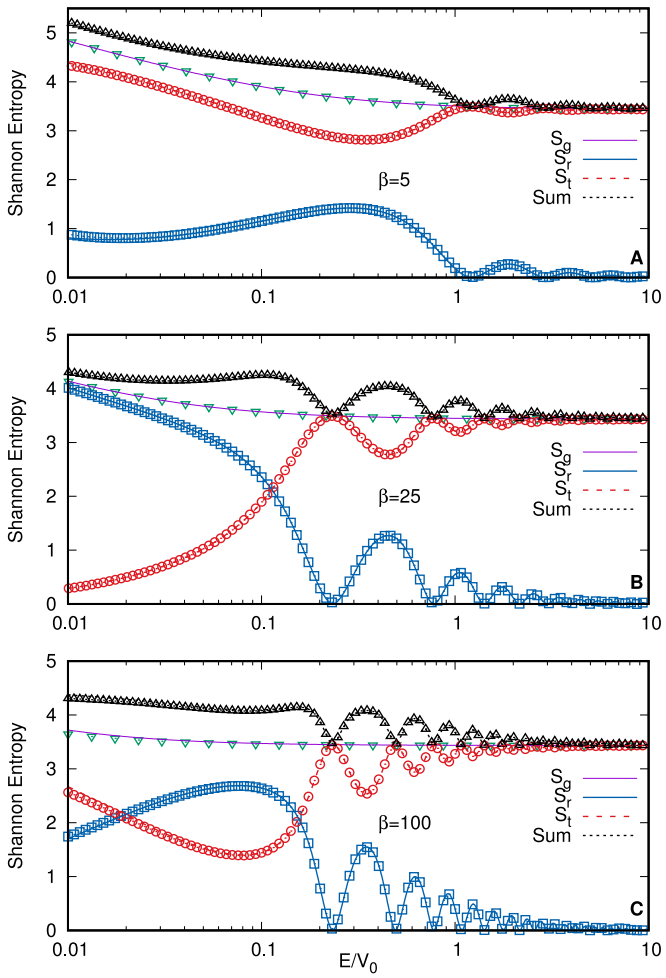

Figure 7. The Shannon entropy components, S_i (i refers to r or t) from equation (35), and total Shannon entropy, $\mathcal{S}_T = S_r + S_t$, as a function of the collision energy $\epsilon = E/V_0$ in the scaled coordinates. Here, S_g corresponds to the results of Shannon entropy for a single Gaussian, as is shown in equation (21) (shown in thin purple line). The reflected contribution, S_r, is shown in solid blue line, while the transmitted, S_t is shown in red dashed line. Finally, the sum (total) Shannon entropy is shown in black dotted line. The same color symbols are the corresponding numerical results. We also compare to the numerical data (open down triangle symbol) from equation (45), equivalent to a Gaussian contribution S_g. In **A**, we show the case $\beta = 5$, in **B**, the case $\beta = 25$, and in **C**, the case $\beta = 100$. See text for discussion.

higher the time t. On the other hand, the trapped entropy S_{tr} exhibits a Gaussian-like profile within the potential well, and the corresponding profile shifts towards the higher time region as ϵ decreases. This behavior is well understood, as the incident wave packet interacts with the potential well within the region $-R_0 < x < R_0$, leading to a transient trapping of probability density. This, in turn, manifests as a temporary contribution to the Shannon entropy S_{tr}, which gradually vanishes as the wave packet escapes the well and continues its propagation.

Next, the detailed variation of the S_r and S_t as a function of ϵ is depicted in figure 7. Here again, the lines are the analytical results from equation (20) while the same color symbols are the numerical results from the finite-difference approach. Evidently, both sets of results are in excellent agreement. Interestingly, we find that both S_r and S_t exhibit oscillatory behavior, with their nodes or anti-nodes occurring at exactly the same energy values as those observed for the R and T coefficients. At low energies with a small effective mass (e.g., $\beta = 5$), the particle is transmitted almost entirely through the potential well due to the near-resonance condition. This results in a more dispersed spatial distribution of the transmitted wave, while the reflected wave packet remains comparatively localized (see the upper panel of figure 1). As a result, the S_t becomes much higher as compared to S_r as clearly depicted from the upper panel of figure 7. As the energy increases with the same β, a portion of the wave packet begins to be reflected back from the potential well. Consequently, S_r attains a high value and then decreases nearly parabolically up to a specific ϵ, beyond which it displays an oscillatory pattern. This can be clearly noted from figure 7. For instance, for $\beta = 5$, the value of S_r is $\approx$0.95 at $\epsilon = 0.01$, which attain a height $S_r \approx 1.5$ at around $\epsilon \approx 0.45$, and then decreases to zero at $\epsilon \approx 1.3$, beyond which S_r follows a decaying oscillatory trend. This suggests that at resonance energies, the reflected Shannon entropy vanishes due to the complete transmission of the wave. This behavior can eventually be interpreted, in an information-theoretic sense, as a

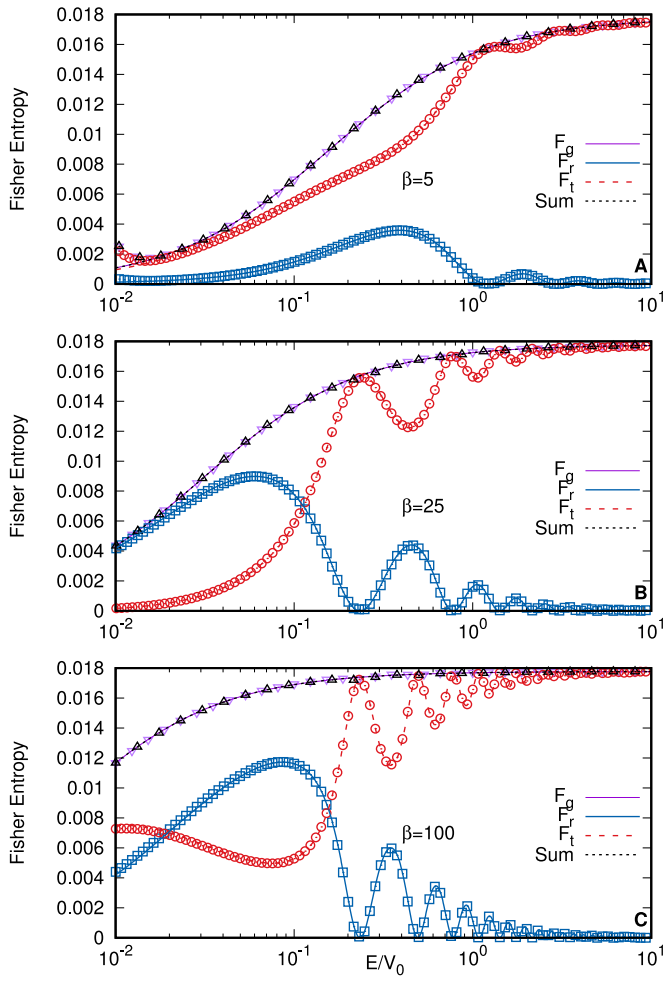

Figure 8. The Fisher entropy, F_i, for the reflected and transmitted contributions, in the scaled coordinates, as a function of the ratio $\epsilon = E/V_0$. The labeling is the same as in figure 7. In **A**, we show the case $\beta = 5$, in **B**, the case $\beta = 25$, and in **C**, the case $\beta = 100$. See text for discussion.

quantitative signature of 'quantum transparency'. While the reflection coefficient R measures the total reflected probability, the entropy S_r characterizes the information content and spatial delocalization of the reflected probability density. The simultaneous collapse of both quantities at resonance indicates the disappearance of reflected information. The energy dependence of S_r near resonance closely follows the resonance profile. In particular, the sharpness of the entropy minimum reflects the resonance width Γ: narrow resonances produce a rapid and localized suppression of S_r, whereas broader resonances yield smoother minima. Since resonance widths are experimentally accessible in atomic, molecular, and nanoparticle scattering via transmission or cross-section measurements, this establishes a natural connection between the entropy behavior and measurable quantities. Furthermore, the stability of a resonance against external perturbations can be inferred from the robustness of the entropy minimum. Stable resonances retain a deep and well-defined minimum in S_r under small parameter variations, whereas fragile resonances show a rapid lifting of the minimum and increased entropy fluctuations. Thus, the behavior of Shannon entropies near resonance provides complementary insight into resonance stability, consistent with, but independent of, traditional lifetime and linewidth analyses. Another interesting observation is the decrease in the peak heights of the antinodes of S_r, along with a reduction in their widths as ϵ increases. This is due to the rapid transmission of the particle through the well. As the collisional energy rises, the kinetic energy of the wave packet increases and therefore the potential well appears to be more transparent. An exactly opposite trend is observed for S_t, while, as expected, S_{tr} remains zero throughout the entire energy range. The overall variation of S_r and S_t for different β closely follows the same trend observed for the reflection and transmission coefficients. It is important to emphasize that neither S_r nor S_t represents the *true* entropy, since, as noted earlier, these quantities are derived from a non-normalized density distributions, but their sum does [see equation (19)]. Their significance may be understood as follows: during the scattering process, a portion of the wave packet is reflected, carrying with it the information content S_r, while the remaining part, S_t, is transmitted through the potential well. Hence, S_r and S_t represent the respective contributions to the Shannon entropy sum, satisfying the relation given by equation (19). The variation of

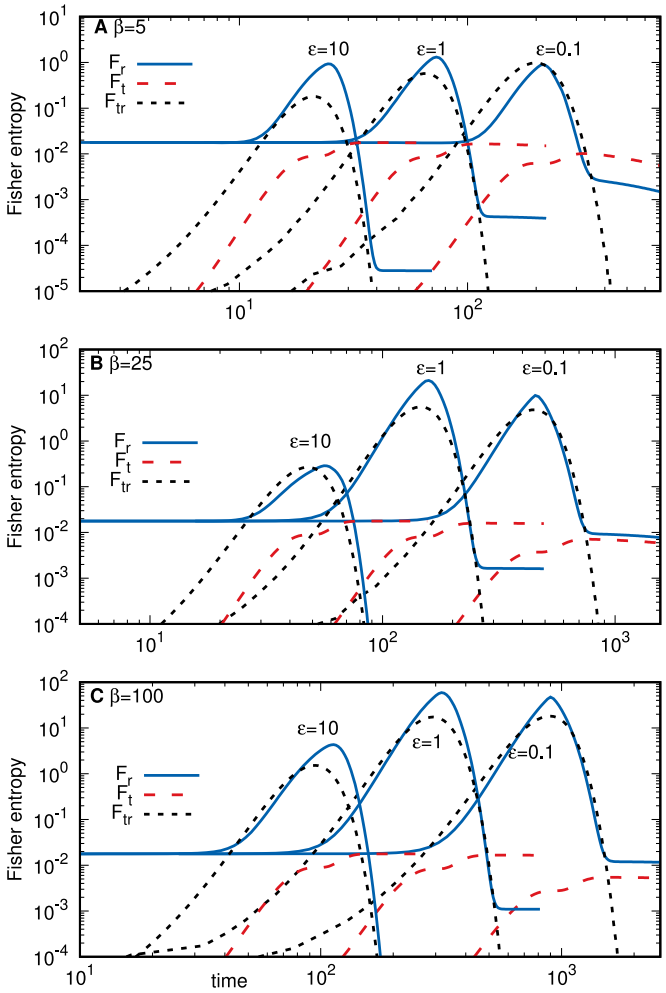

Figure 9. Time evolution of the Fisher entropy, F_i (i refers to r or t or tr) from equation (36), for the three different energies $\epsilon = 0.1$, 1 and 10 in the scaled coordinates. The labeling is the same as in figure 6. In **A**, we show the case $\beta = 5$, in **B**, the case $\beta = 25$, and in **C**, the case $\beta = 100$. See text for discussion.

$\mathcal{S}_T$ as a function of ϵ can be found in figure 7, depicted by the black dotted line ($S_r + S_t$) and black diamond symbol (numerical data). Evidently, it exhibits a very intriguing feature as it demonstrates an oscillatory nature with the positions of minima identical to the reflected S_r entropy. Moreover, the total Shannon entropy of the system for the numerical and analytical approximation reflected and transmitted components agrees very well. This indicates that, except for the low energy, the breaking of the wave packet into two Gaussian waves is a good approximation. In the same figure, just for completeness, we show the single reflected and transmitted Gaussian contribution of equation (21) (purple dotted line) and the numerical results when normalizing the reflected and transmitted wave function [equation (45)] (open down triangle). Thus, the total true Fisher entropy is modulated by those two contributions [see equation (20)].

In addition to the Shannon entropy, we have also evaluated Fisher entropy, F. It is worth noting that, for a stationary state, the Fisher information entropy typically exhibits a conjugate behavior in comparison to its Shannon entropy counterpart. However, this relationship is not necessarily preserved in dynamical systems, particularly in scattering processes where fragmentation is involved. The underlying reasons for this divergence are multifaceted. For example, when a Gaussian wave packet interacts with a square well potential, it experiences interference effects, resulting in partial reflection and transmission of the wave packet. In such scenarios, the Fisher entropy, which serves as a local measure of information and is highly sensitive to the gradient of the probability density, may exhibit behavior analogous to that of the Shannon entropy.

To gain a deeper insight, first, we have plotted the reflected, F_r, and transmitted, F_t, components of Fisher entropy as a function of the energy ϵ, as shown in figure 8. Notably, for low-energy particles ($\epsilon \lesssim 0.08$) with arbitrary β, F_r exhibits an almost conjugate behavior relative to the corresponding Shannon entropy component S_r. However, beyond this energy threshold, we observe that the overall characteristics of F_r, including its oscillatory nature and the positions of its nodes, closely resemble those of S_r. On the contrary, it is observed that F_t for $\epsilon < \epsilon_0$ and arbitrary β behaves almost similarly to that of S_t. The values of ϵ_0 for $\beta = 5$, 25 and 100 where

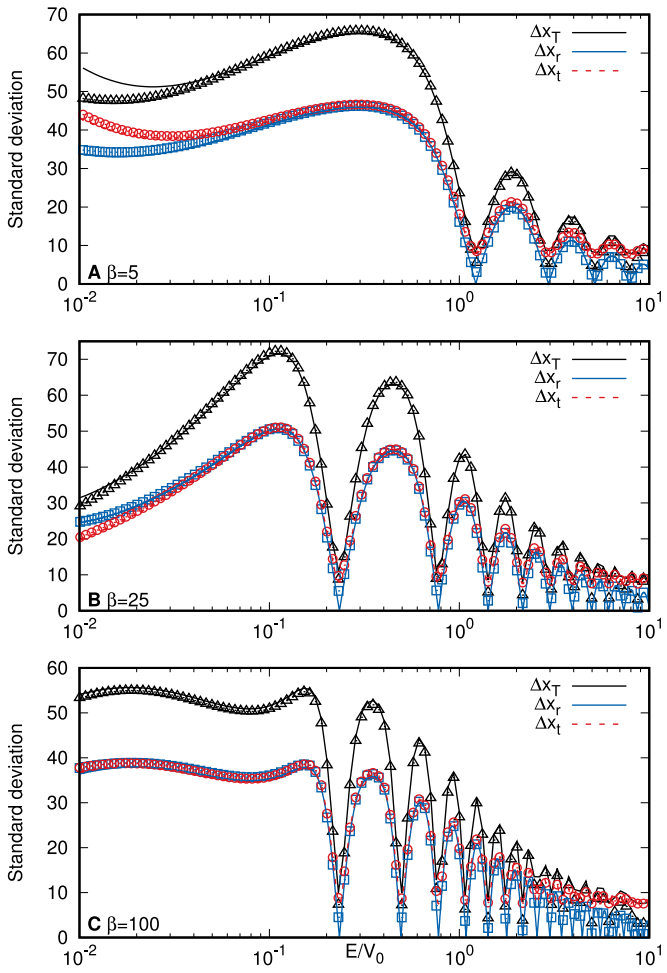

Figure 10. Standard deviation, Δx, in the scaled coordinates, as a function of the ratio $\epsilon = E/V_0$ [see equation (37)]. The labeling is the same as in figure 7. The case for $\beta = 5$ is shown in **A**, for $\beta = 25$ in **B**, and $\beta = 100$ in **C**. See text for discussion.

this occurs, are approximately 1.2, 0.25, and 0.22. Thereafter, for $\epsilon > \epsilon_0$, F_t exhibits oscillations. Unlike S_t, the resonance peaks of F_t increase monotonically and eventually saturate to a nearly constant value at higher energies ($\epsilon > 5$). This behavior can be well understood from basic principles of quantum mechanics. At some low energies ($\epsilon \lesssim 0.1$) with arbitrary β, the incident particle lacks sufficient energy to overcome the potential barrier. As a result, at those energies, the wave packet is mainly reflected, with only a small fraction transmitted through the potential well. This is evident in the Fisher information: F_r is high due to the localized reflected wave, whereas F_t remains very low. In contrast, at higher energies ($\epsilon > 5$), the particle easily overcomes the barrier, and most of the wave packet is transmitted. The transmitted wave becomes increasingly localized in the transmission region, leading to a monotonic rise in F_t, which follows the resonance structure as a function of ϵ.

However, it should also be mentioned here that both F_r and F_t are explicitly functions of t. So the estimation of these values is critical and may differ from the time of evolution. To ensure the consistency of the results, we provided sufficient time to converge the entropy values for any value of ϵ. The variation of the scaled F_r, F_t and F_{tr} as a function of t is demonstrated in figure 9. To clearly illustrate the variation, both axes are presented on a logarithmic scale. We have considered three distinct energy values ($\epsilon = 0.1, 1, 10$) and three effective mass values ($\beta = 5, 25, 100$). It is evident that the convergence of the Fisher information takes a longer time for particles with lower energy. Specifically, the reflected Fisher information, F_r, initially remains nearly constant, followed by a distinct peak, after which it decreases in a step-like manner before finally converging as t increases. In contrast, the transmitted Fisher information, F_t, starts from a very small value for all three energy levels and gradually increases, eventually saturating to a constant value as t increases. The result is consistent for any arbitrary ϵ and β.

Further, the total Fisher entropy, defined as $\mathcal{F}_T$, for the numerical and analytical cases are also evaluated and presented in figure 8. One important observation from this figure is that the numerical and analytical Gaussian approximation coincide with each other for all values of ϵ with arbitrary β. More importantly, unlike the Shannon entropy sum ($\mathcal{S}_T$), the Fisher entropy sum ($\mathcal{F}_T$) is independent of R and T, and varies solely with the width of the wave packet, as confirmed by equation (24).

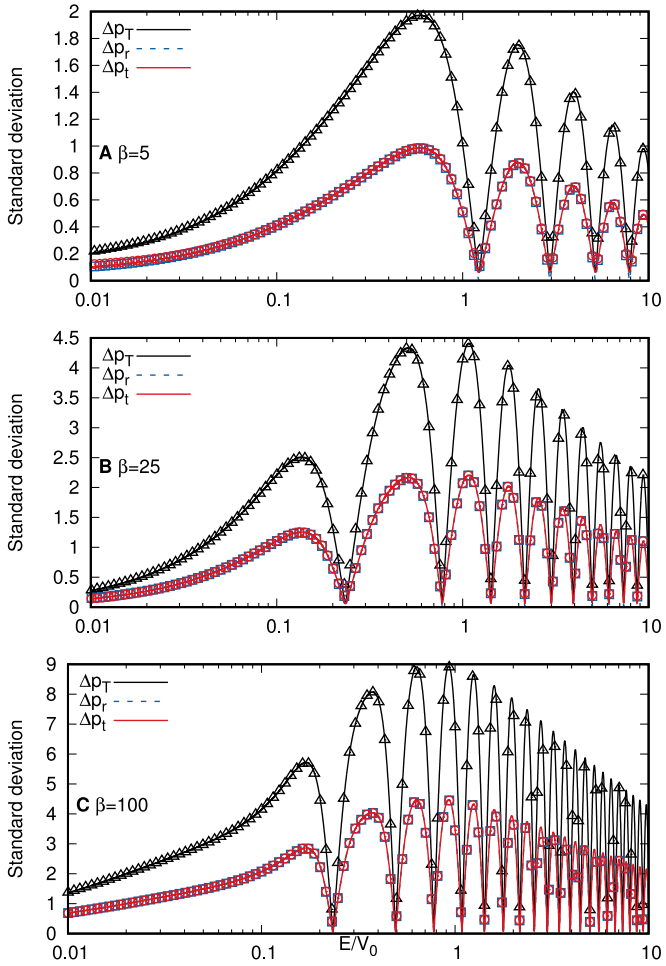

Figure 11. The same as figure 10, but for Δp [see equation (37)].

3.1.3. Standard deviation and uncertainty principle

The analysis of the standard deviations in position, Δx, and momentum, Δp, during a scattering process is crucial for characterizing the position and momentum spread of the wave packet. More specifically, these measures provide insights into the localization and dispersion properties of the wave packet in both position and momentum space.

By employing equation (29), the values of standard deviations in position space, Δx, and momentum space, Δp, are determined with the help of the numerical wave function, while the same is performed with the Gaussian wave function approximation of equation (31). Over the entire energy range (ϵ), the values of Δx for both the reflected (Δx_r) and transmitted (Δx_t) components obtained from the FD technique are in close agreement with those from the Gaussian wave packet. From figure 10(A), it is found that the value of Δx_r is less than that of Δx_t, for $\epsilon < 0.1$ for the case $\beta = 5$. This is because, at such low energy, most of the wave packet is reflected by the potential wall, forming a more localized wave packet, whereas the transmitted part is weak and more dispersed. As ϵ increases, both Δx_r and Δx_t grow monotonically at first, and then exhibit an oscillatory behavior, with minima occurring at the same energy values as observed previously in the context of the RT effect and QIE. Importantly, the minima for Δx_t consistently remain higher than those of Δx_r, supporting the notion of near-complete transmission at those specific energy values, while the nullity of the reflected dispersion is due to the fact that there is no reflected wave packet. However, at high energy with high kinetic energy, we find a significant difference between Δx_r and Δx_t, and particularly $\Delta x_t > \Delta x_r$, indicating near-complete transmission and greater dispersion of the transmitted wave packet. An exactly conjugate nature is observed for both standard momentum deviation Δp_t and Δp_r for $\beta = 5$ as is depicted in figure 11(A). As β increases to 25, it is observed that for low collision energy ($\epsilon < 0.1$), Δx_r begins to dominate over Δx_t, as expected. Even at low energies, the near-resonance condition allows most of the wave packet to transmit through the potential well. Consequently, the reflected wave becomes more dispersed, leading to the dominance of Δx_r. On the other hand, at high energies, the variation follows a similar trend to that for $\beta = 5$, with the only difference being that the number of oscillations increases due to the enlargement of the effective mass β. A similar observation is also

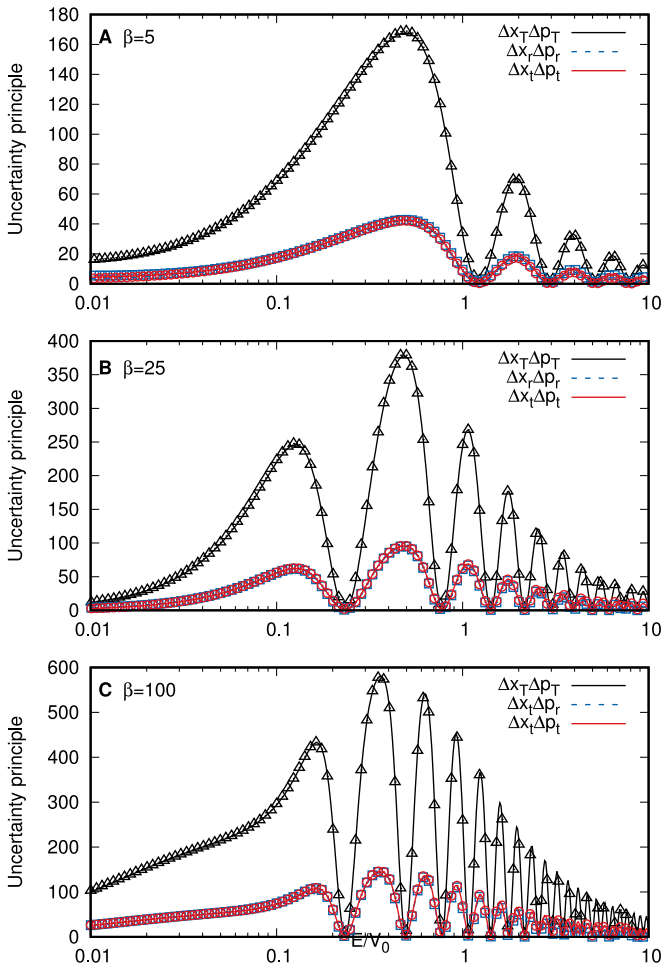

Figure 12. The Heisenberg uncertainty, $\Delta x\Delta p$, as a function of the energy ratio $\epsilon = E/V_0$ for the case $\beta = 5$ in **A**, $\beta = 25$ in **B**, and $\beta = 100$ in **C**. The labeling is the same as in figure 7. See text for discussion.

noted for $\beta = 100$. Another important observation for all β is that at resonances $\Delta x_r \to 0$, while Δx_t remains finite. This is expected because, at resonance, the wave packet undergoes full transmission, leaving no residual reflected component. The total position-space standard deviation, Δx_T, reveals a distinct discrepancy between the FD technique and the Gaussian wave packet for low energies ($\epsilon < 0.1$). Interestingly, such a discrepancy is observed only for small values of β (e.g., $\beta = 5$), while it becomes less pronounced as β increases. This trend is clearly illustrated in figure 10. In contrast, an exactly conjugate trend for all β values is observed in momentum space for both Δp_r and Δp_t. The main reason for this discrepancy is that the approximation of a Gaussian wave packet, as assumed in equations (14) and (15) do not hold anymore. At low collision energy, the reflected wave packet shows several trailing waves from reflection on the two walls of the square well potential [84], well represented by the numerical results.

Next, we study Heisenberg's uncertainty principle [60] that gives the lower bound of the product of the position Δx and momentum Δp uncertainty. Mathematically, this principle can be expressed as

$$\Delta x\Delta p \geqslant \frac{1}{2}. \tag{46}$$

In this study, we have evaluated this uncertainty product for both reflected and transmitted components of the wave packet for various energies of the incident particle to gain deeper insight into the underlying quantum behavior during scattering dynamics. In figure 12, the variation of the uncertainty relation for both reflected and transmitted wave packets is presented as a function of the energy ϵ for $\beta = 5$, 25 and 100. It is observed that for $\beta = 5$ and $\epsilon < 0.1$, the uncertainty for the transmitted wave packet dominates over the reflected part. As earlier discussed, in the low energy limits Δx_r dominates over Δx_t, and conjugately Δp_t dominates over Δp_r. But, due to conservation of energy, $\Delta p_r = \Delta p_t < 1$, while $\Delta x_r = \Delta x_t \gg 1$. Therefore, overall, the product exhibits a trend similar to that of Δx_r or Δx_t. As the energy increases beyond $\epsilon = 0.1$, a sharp peak appears near $\epsilon \approx 0.5$, followed by a step-like decrease, reaching its minimum around $\epsilon \approx 1.1$. Beyond $\epsilon = 1.2$, the uncertainty exhibits an oscillatory behavior, with nodes occurring precisely at the same energies as those identified for the

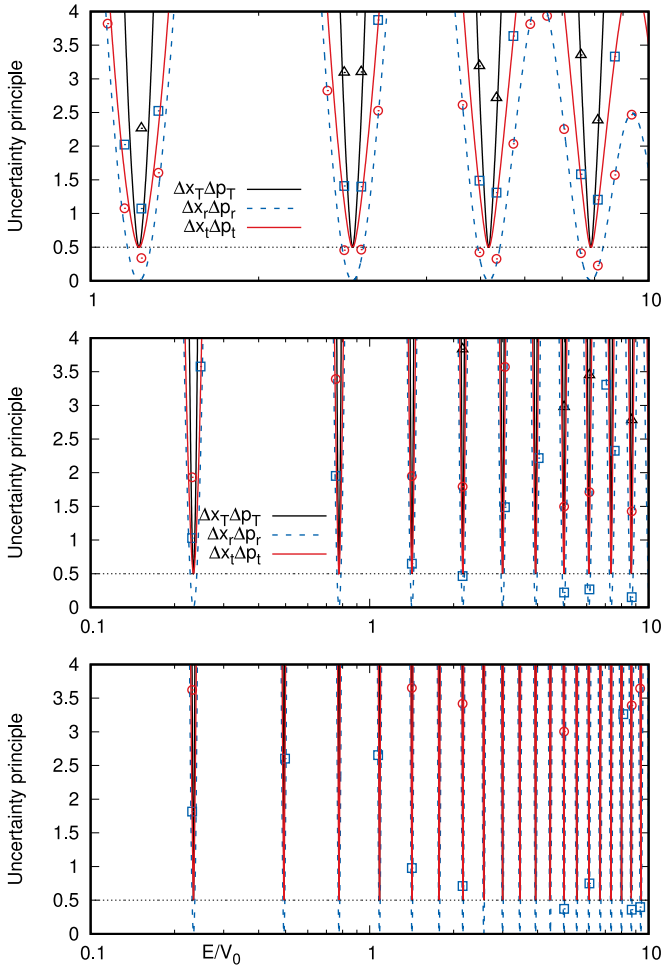

Figure 13. Zoom of figure 12 showing the behavior of Heisenberg uncertainty principle for the reflected and transmitted wave packet. Note that the transmitted wave packet fulfills the minimum uncertainty for full transmission, as shown by the dotted line, while the reflected becomes null. See text for discussion.

RT variation. However, for $\beta = 25$, the first peak occurs near $\epsilon \approx 0.13$, with $\Delta x_r \Delta p_r \approx \Delta x_t \Delta p_t \approx 65$, while the second peak appears around $\epsilon \approx 0.5$, where $\Delta x_r \Delta p_r \approx \Delta x_r \Delta p_t \approx 97$. This indicates that, at $\epsilon \approx 0.13$, the wave packet is less dispersed compared to the case at $\epsilon \approx 0.5$, as is also indicated from the density profile presented in figure 2. Beyond this, the behavior becomes monotonic, with the peak heights decreasing as the collisional energy increases, suggesting that the wave packet becomes progressively more localized. An identical pattern of uncertainty variation is observed for $\beta = 100$.

Another important observation is that, irrespective of the value of β, the uncertainty at resonances is exactly zero for the normalized reflected wave packet, while it is exactly 0.5 for the normalized transmitted wave packet, at the resonance of the RT effect. This behavior can be clearly visualized in figure 13 and can be well explained by recalling equation (32). At resonances, $R = 0$, which gives $\Delta x_r \Delta p_r = 0$, independent of β. In contrast, since $T = 1$ at resonances, and a simple analytical calculation shows that $\Delta x_t \, \Delta p_t \, = \frac{1}{2}$, which is also independent of β. This is well known for a Gaussian wave packet, which is a coherent state and satisfies the minimum of uncertainty [79]. Intriguingly, near the resonances where $R \neq 0$ but $R \to 0$, we find that $\Delta x_r \, \Delta p_r \, < \frac{1}{2}$, while $\Delta x_t \, \Delta p_t \, > \frac{1}{2}$. For instance, at $\beta = 5$ for $\epsilon = 8.111$, the corresponding values of $\Delta x_r \Delta p_r = 0.2255$ and $\Delta x_t \Delta p_t = 1.2044$. Similarly, the values of $\Delta x_r \Delta p_r = 0.2482$ at $\epsilon = 10.0$ for $\beta = 25$, while $\Delta x_t \Delta p_t = 1.8648$. Thus, it is evident that, at certain values of ϵ, close to the resonance position for a β, the values of $\Delta x_r \Delta p_r$ appear to violate the Heisenberg uncertainty principle. This is because at these points, the quasi-resonance condition is satisfied and therefore most part of the wave packet is transmitted through the potential well, a feeble part of which is reflected back. However, the total uncertainty, i.e. $\Delta x_T \Delta p_T$, always satisfies the uncertainty principle.

Finally, a selected set of data presented in this work is provided in tables 1–3 for $\beta = 5$, 25, and 100, respectively, for compilation and reference purposes.

Table 1. Reflection and transmission coefficients (R and T), scaled Shannon entropy (S_r and S_t), scaled Fisher entropy (F_r and F_t), position variance (Δx_r and Δx_t), and momentum variance (Δp_r and Δp_t) for different collisional energy ϵ for $\beta = 5$. The notation $a(b)$ stands for $a \times 10^b$.

ϵ	R	T	S_r	S_t	F_r	F_t	Δx_r	Δx_t	Δp_r	Δp_t
0.010	1.2588(−1)	8.7400(−1)	8.7361(−1)	4.3233(+0)	3.2834(−4)	2.1947(−3)	3.4813(+1)	4.3998(+1)	1.0576(−1)	1.2333(−1)
0.014	1.1991(−1)	8.8007(−1)	8.1701(−1)	4.2150(+0)	2.0805(−4)	1.5370(−3)	3.4255(+1)	4.0934(+1)	1.2427(−1)	1.3748(−1)
0.020	1.2153(−1)	8.7847(−1)	8.0591(−1)	4.0751(+0)	2.4776(−4)	1.8336(−3)	3.4413(+1)	3.9100(+1)	1.4911(−1)	1.5909(−1)
0.028	1.2985(−1)	8.7015(−1)	8.3204(−1)	3.9155(+0)	3.5782(−4)	2.4242(−3)	3.5251(+1)	3.8432(+1)	1.8242(−1)	1.8963(−1)
0.040	1.4468(−1)	8.5532(−1)	8.9032(−1)	3.7423(+0)	5.3359(−4)	3.1621(−3)	3.6693(+1)	3.8787(+1)	2.2670(−1)	2.3155(−1)
0.057	1.6600(−1)	8.3400(−1)	9.7642(−1)	3.5598(+0)	8.0029(−4)	4.0168(−3)	3.8593(+1)	3.9943(+1)	2.8459(−1)	2.8760(−1)
0.081	1.9333(−1)	8.0667(−1)	1.0844(+0)	3.3727(+0)	1.1871(−3)	4.9450(−3)	4.0759(+1)	4.1626(+1)	3.5857(−1)	3.6024(−1)
0.100	2.1202(−1)	7.8798(−1)	1.1556(+0)	3.2610(+0)	1.4854(−3)	5.5133(−3)	4.2069(+1)	4.2742(+1)	4.1143(−1)	4.1255(−1)
0.142	2.4474(−1)	7.5526(−1)	1.2749(+0)	3.0831(+0)	2.0863(−3)	6.4359(−3)	4.4085(+1)	4.4550(+1)	5.1409(−1)	5.1470(−1)
0.201	2.7425(−1)	7.2575(−1)	1.3745(+0)	2.9308(+0)	2.7607(−3)	7.3120(−3)	4.5598(+1)	4.5962(+1)	6.3399(−1)	6.3457(−1)
0.285	2.9069(−1)	7.0931(−1)	1.4201(+0)	2.8317(+0)	3.3553(−3)	8.2050(−3)	4.6259(+1)	4.6607(+1)	7.6713(−1)	7.6818(−1)
0.404	2.7844(−1)	7.2156(−1)	1.3571(+0)	2.8284(+0)	3.5831(−3)	9.3215(−3)	4.5504(+1)	4.5916(+1)	9.0035(−1)	9.0240(−1)
0.572	2.1620(−1)	7.8380(−1)	1.0996(+0)	2.9741(+0)	3.0205(−3)	1.1027(−2)	4.1611(+1)	4.2205(+1)	9.8294(−1)	9.8664(−1)
0.811	9.6681(−2)	9.0332(−1)	5.6701(−1)	3.2711(+0)	1.4226(−3)	1.3529(−2)	2.9657(+1)	3.0721(+1)	8.3784(−1)	8.4396(−1)
1.000	2.6955(−2)	9.7304(−1)	1.9270(−1)	3.4375(+0)	3.9120(−4)	1.4993(−2)	1.6135(+1)	1.8098(+1)	5.0763(−1)	5.1610(−1)
1.417	1.1813(−2)	9.8819(−1)	9.4176(−2)	3.4562(+0)	1.7213(−4)	1.5841(−2)	1.0980(+1)	1.3379(+1)	4.0922(−1)	4.1170(−1)
2.009	3.9518(−2)	9.6048(−1)	2.6520(−1)	3.3715(+0)	6.4069(−4)	1.5887(−2)	1.9565(+1)	2.0945(+1)	8.7167(−1)	8.7457(−1)
2.848	8.7433(−4)	9.9913(−1)	9.3900(−3)	3.4580(+0)	9.9993(−6)	1.6853(−2)	2.9195(+0)	8.2433(+0)	1.5554(−1)	1.7080(−1)
4.037	1.2085(−2)	9.8792(−1)	9.5241(−2)	3.4224(+0)	2.0177(−4)	1.6934(−2)	1.0929(+1)	1.3281(+1)	6.9205(−1)	6.9549(−1)
5.722	2.6961(−3)	9.9730(−1)	2.5334(−2)	3.4403(+0)	4.3659(−5)	1.7274(−2)	5.1971(+0)	9.1773(+0)	3.9164(−1)	3.9627(−1)
8.111	2.4910(−4)	9.9975(−1)	2.9682(−3)	3.4424(+0)	3.1173(−6)	1.7450(−2)	1.5866(+0)	7.7287(+0)	1.4215(−1)	1.5583(−1)
10.000	1.6597(−3)	9.9834(−1)	1.6371(−2)	3.4371(+0)	2.7849(−5)	1.7490(−2)	4.0355(+0)	8.5560(+0)	4.0388(−1)	4.0958(−1)

Table 2. Same as table 1 but for $\beta = 25$.

ϵ	R	T	S_r	S_t	F_r	F_t	Δx_r	Δx_t	Δp_r	Δp_t
0.010	9.6069(−1)	3.9312(−2)	4.0139(+0)	2.8973(−1)	4.1766(−3)	1.7246(−4)	2.4754(+1)	2.0494(+1)	1.5206(−1)	1.4040(−1)
0.014	9.4479(−1)	5.5207(−2)	3.8442(+0)	3.8129(−1)	5.2847(−3)	3.1021(−4)	2.6641(+1)	2.3866(+1)	2.0275(−1)	1.9523(−1)
0.020	9.2243(−1)	7.7573(−2)	3.6710(+0)	5.0071(−1)	6.4691(−3)	5.4497(−4)	2.9540(+1)	2.7762(+1)	2.7545(−1)	2.7106(−1)
0.028	8.9072(−1)	1.0928(−1)	3.4882(+0)	6.5722(−1)	7.6074(−3)	9.3353(−4)	3.3336(+1)	3.2222(+1)	3.7728(−1)	3.7523(−1)
0.040	8.4496(−1)	1.5504(−1)	3.2832(+0)	8.6535(−1)	8.5247(−3)	1.5640(−3)	3.7917(+1)	3.7257(+1)	5.1741(−1)	5.1718(−1)
0.057	7.7645(−1)	2.2355(−1)	3.0295(+0)	1.1506(+0)	8.9822(−3)	2.5867(−3)	4.3093(+1)	4.2769(+1)	7.0642(−1)	7.0774(−1)
0.081	6.6773(−1)	3.3227(−1)	2.6698(+0)	1.5601(+0)	8.6113(−3)	4.2916(−3)	4.8278(+1)	4.8244(+1)	9.4879(−1)	9.5173(−1)
0.100	5.6986(−1)	4.3014(−1)	2.3538(+0)	1.8970(+0)	7.7445(−3)	5.8639(−3)	5.0499(+1)	5.0647(+1)	1.1062(+0)	1.1103(+0)
0.142	3.2410(−1)	6.7590(−1)	1.5113(+0)	2.6514(+0)	4.6944(−3)	9.8924(−3)	4.7312(+1)	4.7857(+1)	1.2422(+0)	1.2489(+0)
0.201	4.3598(−2)	9.5640(−1)	2.9170(−1)	3.3967(+0)	6.0570(−4)	1.4690(−2)	2.0337(+1)	2.2032(+1)	6.4020(−1)	6.5060(−1)
0.285	6.7627(−2)	9.3237(−1)	4.1981(−1)	3.3165(+0)	1.0243(−3)	1.4905(−2)	2.5583(+1)	2.6416(+1)	9.5223(−1)	9.4899(−1)
0.404	2.5015(−1)	7.4985(−1)	1.2158(+0)	2.8175(+0)	4.0976(−3)	1.2414(−2)	4.3910(+1)	4.4195(+1)	1.9459(+0)	1.9452(+0)
0.572	1.8215(−1)	8.1784(−1)	9.4157(−1)	2.9931(+0)	3.0358(−3)	1.3834(−2)	3.8972(+1)	3.9508(+1)	2.0606(+0)	2.0642(+0)
0.811	7.3297(−3)	9.9267(−1)	6.2412(−2)	3.4355(+0)	9.4762(−5)	1.6967(−2)	8.6770(+0)	1.1453(+1)	5.4669(−1)	5.4655(−1)
1.000	9.5106(−2)	9.0489(−1)	5.5262(−1)	3.2106(+0)	1.6117(−3)	1.5635(−2)	2.9515(+1)	3.0265(+1)	2.0723(+0)	2.0722(+0)
1.417	7.6532(−4)	9.9923(−1)	8.3418(−3)	3.4433(+0)	3.4588(−5)	1.7369(−2)	2.7896(+0)	8.0692(+0)	2.3260(−1)	2.4156(−1)
2.009	1.2860(−2)	9.8714(−1)	1.0071(−1)	3.4099(+0)	2.0956(−4)	1.7287(−2)	1.1222(+1)	1.3498(+1)	1.1235(+0)	1.1279(+0)
2.848	5.7750(−3)	9.9423(−1)	4.9912(−2)	3.4251(+0)	9.2051(−5)	1.7488(−2)	7.5256(+0)	1.0635(+1)	8.9843(−1)	9.0281(−1)
4.037	1.5728(−3)	9.9843(−1)	1.5718(−2)	3.4338(+0)	2.2709(−5)	1.7617(−2)	3.9509(+0)	8.4829(+0)	5.6113(−1)	5.6345(−1)
5.722	4.7482(−3)	9.9525(−1)	4.1818(−2)	3.4247(+0)	8.0577(−5)	1.7606(−2)	6.7765(+0)	1.0097(+1)	1.1522(+0)	1.1548(+0)
8.111	3.1811(−3)	9.9682(−1)	2.9277(−2)	3.4278(+0)	5.4448(−5)	1.7661(−2)	5.5451(+0)	9.3179(+0)	1.1201(+0)	1.1223(+0)
10.000	1.1626(−4)	9.9988(−1)	1.4816(−3)	3.4350(+0)	1.3444(−6)	1.7726(−2)	1.0478(+0)	7.5826(+0)	2.3689(−1)	2.4593(−1)

Table 3. Same as table 1 but for $\beta = 100$.

ϵ	R	T	S_r	S_t	F_r	F_t	Δx_r	Δx_t	Δp_r	Δp_t
0.010	3.7726(−1)	6.2274(−1)	1.7427(+0)	2.5644(+0)	4.4010(−3)	7.2693(−3)	3.7732(+1)	3.7815(+1)	6.8814(−1)	6.8660(−1)
0.014	4.4362(−1)	5.5638(−1)	1.9538(+0)	2.3241(+0)	5.7553(−3)	7.2246(−3)	3.8644(+1)	3.8606(+1)	8.3883(−1)	8.3703(−1)
0.020	5.1388(−1)	4.8612(−1)	2.1664(+0)	2.0761(+0)	7.2420(−3)	6.8578(−3)	3.8877(+1)	3.8742(+1)	1.0039(+0)	1.0021(+0)
0.028	5.8238(−1)	4.1762(−1)	2.3640(+0)	1.8338(+0)	8.7412(−3)	6.2752(−3)	3.8388(+1)	3.8169(+1)	1.1787(+0)	1.1769(+0)
0.040	6.4241(−1)	3.5759(−1)	2.5295(+0)	1.6173(+0)	1.0107(−2)	5.6331(−3)	3.7358(+1)	3.7067(+1)	1.3633(+0)	1.3618(+0)
0.057	6.8621(−1)	3.1379(−1)	2.6448(+0)	1.4547(+0)	1.1176(−2)	5.1190(−3)	3.6207(+1)	3.5865(+1)	1.5709(+0)	1.5698(+0)
0.081	7.0216(−1)	2.9784(−1)	2.6814(+0)	1.3925(+0)	1.1726(−2)	4.9851(−3)	3.5677(+1)	3.5331(+1)	1.8426(+0)	1.8422(+0)
0.100	6.8801(−1)	3.1199(−1)	2.6374(+0)	1.4423(+0)	1.1622(−2)	5.2851(−3)	3.6079(+1)	3.5776(+1)	2.0724(+0)	2.0725(+0)
0.142	5.7003(−1)	4.2997(−1)	2.2887(+0)	1.8465(+0)	9.7550(−3)	7.3964(−3)	3.8272(+1)	3.8202(+1)	2.6352(+0)	2.6373(+0)
0.201	1.4391(−1)	8.5609(−1)	7.7770(−1)	3.0845(+0)	2.4017(−3)	1.4808(−2)	2.6722(+1)	2.7578(+1)	2.2194(+0)	2.2264(+0)
0.285	2.0082(−1)	7.9918(−1)	1.0157(+0)	2.9307(+0)	3.4389(−3)	1.3951(−2)	3.0694(+1)	3.1180(+1)	3.0260(+0)	3.0226(+0)
0.404	2.4624(−1)	7.5376(−1)	1.1936(+0)	2.8054(+0)	4.2727(−3)	1.3261(−2)	3.2911(+1)	3.3373(+1)	3.8677(+0)	3.8710(+0)
0.572	1.4881(−1)	8.5119(−1)	7.9653(−1)	3.0634(+0)	2.5742(−3)	1.5014(−2)	2.7144(+1)	2.7833(+1)	3.8078(+0)	3.8058(+0)
0.811	2.3341(−2)	9.7666(−1)	1.6918(−1)	3.3808(+0)	3.7087(−4)	1.7223(−2)	1.1497(+1)	1.3608(+1)	1.9258(+0)	1.9228(+0)
1.000	6.3706(−2)	9.3629(−1)	3.9535(−1)	3.2790(+0)	1.0921(−3)	1.6570(−2)	1.8513(+1)	1.9815(+1)	3.4483(+0)	3.4518(+0)
1.417	7.6104(−4)	9.9924(−1)	8.2929(−3)	3.4345(+0)	3.5715(−5)	1.7682(−2)	2.1090(+0)	7.7977(+0)	4.6405(−1)	4.6849(−1)
2.009	3.4175(−2)	9.6583(−1)	2.3324(−1)	3.3510(+0)	5.9019(−4)	1.7144(−2)	1.3722(+1)	1.5519(+1)	3.6347(+0)	3.6365(+0)
2.848	1.6814(−2)	9.8319(−1)	1.2674(−1)	3.3935(+0)	2.8834(−4)	1.7456(−2)	9.6803(+0)	1.2173(+1)	3.0602(+0)	3.0621(+0)
4.037	4.8392(−3)	9.9516(−1)	4.2588(−2)	3.4227(+0)	8.0120(−5)	1.7671(−2)	5.2212(+0)	9.1080(+0)	1.9665(+0)	1.9663(+0)
5.722	5.2155(−3)	9.9478(−1)	4.5422(−2)	3.4215(+0)	8.9257(−5)	1.7673(−2)	5.3929(+0)	9.2058(+0)	2.4257(+0)	2.4261(+0)
8.111	1.0913(−3)	9.9891(−1)	1.1243(−2)	3.4315(+0)	1.7623(−5)	1.7748(−2)	2.4687(+0)	7.8892(+0)	1.3216(+0)	1.3224(+0)
10.000	3.8254(−4)	9.9962(−1)	4.3585(−3)	3.4332(+0)	5.6812(−6)	1.7762(−2)	1.4544(+0)	7.6389(+0)	8.6656(−1)	8.6969(−1)

4. Conclusion

In this work, we have investigated the behavior of reflection and transmission coefficients, information entropy (Shannon and Fisher entropy), and Heisenberg's uncertainty principle on the scattering of a free particle impacting an impurity, modeled by a finite square well potential. By applying a suitable scaling transformation, we rewrite the Schrödinger equation in terms of an effective mass, $\beta = mV_0R_0^2$, and the energy ratio, $\epsilon = E/V_0$. The effective mass, which in principle depends on the width and depth of the potential as well as the mass of the free particle, provides a universal scaling of the physical properties. Importantly, this approach eliminates the need to consider all possible combinations of well parameters to study the system dynamics. The Schrödinger equation is solved using the Finite-Difference approach in conjunction with the split-operator technique to investigate the dynamics of the system. The well-known Ramsauer–Townsend (RT) effect is observed as a function of the energy ϵ by estimating the reflection, R, transmission, T, and trapped, T_{tr} coefficients of the wave packet. It is found that the effective mass governs the RT effect, with the number of resonances increasing as the effective mass increases. For the first time in the literature, we have investigated quantum information measures, such as Shannon and Fisher entropy, as functions of the energy ϵ for a dynamical scattering process. We find that both Shannon and Fisher entropy for reflected as well as for transmitted wave packets can effectively capture the delocalization or localization characteristics of the wave packet scattered by the square well when fragmentation is occurring. An oscillatory behavior is also observed for both Shannon and Fisher information entropy, with the number of oscillations being controlled by the effective mass β, which dictates the RT behavior. Unlike most quantum systems where Shannon and Fisher entropy exhibit conjugate behavior, here we observe that they vary similarly with respect to the energy ϵ. The standard deviations in both position and momentum space, as functions of the energy ϵ, exhibit distinctive features and demonstrate the variation in the overall dispersion of the wave packet as a function of ϵ. Additionally, we have examined the most fundamental principles of quantum mechanics, namely the Heisenberg uncertainty principle, as a function of the effective mass. For a given value of the effective mass, at certain energies, the uncertainty for the normalized reflected wave packet falls below the lower bound, whereas the uncertainty for the normalized transmitted wave packet remains valid across the entire energy range. We find that it is inevitable due to the presence of quasi-resonances at which a very tiny part of the wave packet is reflected back. All these previous results are validated through analytical expressions based on the reflected and transmitted coefficients for Gaussian wave packets.

In closing, the model problem studied here is fundamentally important, not only because the scaling parameters allow flexibility for arbitrary potential values, but also because the approach can be readily extended to real atomic systems. For instance, the square well potential can serve as a simplified model for a quantum dot, enabling the study of how an incoming electron scatters from the quantum dot's effective potential, including resonances and transmission properties. Moreover, quantum information measures provide a valuable tool for understanding the stability and overall charge distribution of an atom during scattering by an incident particle in a more explicit manner. In this regard, a detailed study on the effectiveness of quantum information measures in real atomic scattering processes is currently in progress. Finally, we hope that the present study provides substantial insights into the fundamental properties of a particle scattered by a square well potential and it paves the way for future research in scattering and fragmentation theory.

Acknowledgments

RCT acknowledges support from PAPIIT-DGAPA-UNAM with grant number IN-109-623. The postdoctoral stay of SM is supported by the DGAPA-UNAM Postdoctoral Scholarship Program.

Data availability statement

All data that support the findings of this study are included within the article (and any supplementary files).

Author contributions

Santanu Mondal 0000-0001-5921-8870
Conceptualization (equal), Data curation (equal), Formal analysis (lead), Funding acquisition (equal), Investigation (lead), Methodology (equal), Resources (equal), Software (equal), Supervision (equal), Validation (equal), Visualization (equal), Writing – original draft (lead), Writing – review & editing (lead)

R Cabrera-Trujillo 0000-0002-1937-2686

Conceptualization (equal), Data curation (equal), Formal analysis (supporting), Funding acquisition (equal), Investigation (supporting), Methodology (equal), Resources (equal), Software (equal), Supervision (equal), Validation (equal), Visualization (equal), Writing – original draft (supporting), Writing – review & editing (supporting)

References

[1] Schiff L I 1981 *Quantum Mechanics* 3rd edn (McGraw-Hill)
[2] Brouard S, Sala R and Muga J G 1994 *Phys. Rev. A* **49** 4312
[3] Krenzlin H M, Budczies J and Kehr K W 1996 *Phys. Rev. A* **53** 3749
[4] Xavier A L and de Aguiar M A M 1997 *Physical Review Letter* **79** 3323
[5] de Aquino V M, Aguilera-Navarro V C, Goto M and Iwamoto H 1998 *Phys. Rev. A* **58** 4359
[6] Abolhasani M and Golshani M 2000 *Phys. Rev. A* **62** 012106
[7] Hartman T E 1962 *J. Appl. Phys.* **33** 3427
[8] Pérez Prieto A L, Brouard S and Muga J G 2001 *Phys. Rev. A* **64** 012710
[9] Ramsauer C 1921 *Ann. Phys., Lpz.* **369** 513
[10] Townsend J and Bailey V 1921 *The London, Edinburgh, and Dublin Philosophical Magazine and Journal of Science* **42** 873
[11] Mott N and Massey H 1965 *The Theory of Atomic Collisions* 3rd edn (Oxford at the Clarendon Press) ch 18
[12] Brode R B 1933 *Review on Modern Physics* **5** 257
[13] Kauppila W E, Stein T S and Jesion G 1976 *Phys. Rev. Lett.* **36** 580
[14] Kukolich S G 1968 *Am. J. Phys.* **36** 701
[15] Mulhauser F *et al* 2001 *Hyperfine Interact.* **138** 41
[16] Aufm Kampe W, Oates D, Schrader W and Bennewitz H 1973 *Chem. Phys. Lett.* **18** 323
[17] Hanham M L and Pettifer R F 2001 *Phys. Rev. B* **64** 180101
[18] Sobhani H and Hassanabadi H 2017 *Indian J. Phys.* **91** 1205
[19] Vahedi J, Nozari K and Pedram P 2012 *Gravitation Cosmol.* **18** 211
[20] Chung W S, Sobhani H and Hassanabadi H 2017 *The European Physical Journal Plus* **132** 398
[21] Sobhani H, Hassanabadi H and Chung W S 2017 *The European Physical Journal C* **77** 425
[22] Sobhani H and Hassanabadi H 2024 *Indian J. Phys.* **98** 2087
[23] Goldberg A, Schey H M and Schwartz J L 1967 *Am. J. Phys.* **35** 177
[24] Nielsen M A and Chuang I L 2010 *Quantum Computation and Quantum Information: 10th Anniversary Edition* (Cambridge University Press)
[25] Shannon C E 1948 *The Bell System Technical Journal* **27** 379
[26] Savage L J 1976 *The Annals of Statistics* **4** 441
[27] Savage L J 1949 *The Mathematical Theory of Communication, by ce Shannon (and Recent Contributions to the Mathematical Theory of Communication) w. Weaver* (University of Illinois Press)
[28] Fisher R A 1992 Statistical methods for research workers *Breakthroughs in Statistics: Methodology and Distribution* ed S Kotz and N L Johnson (Springer) p 66
[29] Hô M, Sagar R P, Schmider H, Weaver D F and Smith V H Jr. 1995 *Int. J. Quantum Chem.* **53** 627
[30] López-Rosa S, Esquivel R O, Angulo J C, Antolín J, Dehesa J S and Flores-Gallegos N 2010 *J. Chem. Theory Comput.* **6** 145
[31] Delle Site L 2009 *Europhys. Lett.* **86** 40004
[32] Massen S E 2003 *Phys. Rev. C* **67** 014314
[33] Guevara N L, Sagar R P and Esquivel R O 2005 *J. Chem. Phys.* **122** 084101
[34] Grassi A 2011 *Int. J. Quantum Chem.* **111** 2390
[35] Paris M G A 2009 *International Journal of Quantum Information* **7** 125
[36] Flores-Gallegos N 2016 *Chem. Phys. Lett.* **666** 62
[37] Guevara N L, Sagar R P and Esquivel R O 2003 *Phys. Rev. A* **67** 012507
[38] González-Férez R and Dehesa J S 2005 *The European Physical Journal D - Atomic, Molecular, Optical and Plasma Physics* **32** 39
[39] Angulo J, Antolín J and Sen K 2008 *Phys. Lett. A* **372** 670
[40] Nalewajski R F 2006 *Information Theory of Molecular Systems* (Elsevier)
[41] Saha S and Jose J 2020 *Phys. Rev. A* **102** 052824
[42] Das Chakladar K, Mondal S, Bhattacharyya S and Saha J K 2025 *Suplemento de la Revista Mexicana de Física* **6** 011305 1–9
[43] Mondal S, Saha J K, Mukherjee P K and Fricke B 2023 *Phys. Scr.* **98** 045411
[44] Mondal S, Chaudhuri S K, Saha J K, Mukherjee P K and Fricke B 2024 *Eur. Phys. J. D* **78** 61
[45] Chakladar K D, Mondal S, Sen K and Saha J K 2024 *Phys. Rev. A* **110** 042819
[46] Mondal S, Sadhukhan A, Sen K and Saha J K 2023 *J. Phys. B: At. Mol. Opt. Phys.* **56** 155001
[47] Chakladar K D, Mondal S, Bhattacharyya S, Sen K and Saha J K 2025 *J. Phys. B: At. Mol. Opt. Phys.* **58** 075003
[48] Estañón C R, Montgomery H E Jr, Angulo J C and Aquino N 2024 *Int. J. Quantum Chem.* **124** e27358
[49] Nascimento W S and Prudente F V 2018 *Chem. Phys. Lett.* **691** 401
[50] Mondal S, Nayek S K and Saha J K 2022 *The European Physical Journal Plus* **137** 373
[51] Verma N and Joshi R 2023 *Phys. Plasmas* **30** 063905
[52] Mondal S, Sen K and Saha J K 2022 *Phys. Rev. A* **105** 032821
[53] Mondal S, Sadhukhan A, Saha J K and Roy A K 2024 *J. Phys. B: At. Mol. Opt. Phys.* **57** 175001
[54] Mondal S, Saha J K and Roy A K 2025 *Int. J. Quantum Chem.* **125** e70056
[55] Nascimento W, Maniero A, Prudente F, de Carvalho C and Jalbert G 2024 *Physica B* **677** 415692
[56] Nascimento W, Maniero A, Prudente F, de Carvalho C and Jalbert G 2025 *Physica B* **699** 416769
[57] Ou J-H and Ho Y K 2017 *Atoms* **5** 15
[58] Mondal S, Sadhukhan A, Sen K and Saha J K 2023 *The European Physical Journal Plus* **138** 576
[59] Sarswat S, Aiswarya R and Jose J 2022 *Physics B: Atomic, Molecular and Optical Physics* **55** 055003
[60] Heisenberg W 1927 *Zeitschrift für Physik* **43** 172

[61] Zheng X, Ma S-Q, Zhang G-F, Fan H and Liu W-M 2020 *Sci. Rep.* **10** 150
[62] Hofmann H F and Takeuchi S 2003 *Phys. Rev. A* **68** 032103
[63] Liu S, Mu L-Z and Fan H 2015 *Phys. Rev. A* **91** 042133
[64] Schwonnek R, Dammeier L and Werner R F 2017 *Phys. Rev. Lett.* **119** 170404
[65] Wootters W K and Zurek W H 1982 *Nature* **299** 802
[66] Dieks D 1982 *Phys. Lett. A* **92** 271
[67] Gisin N, Ribordy G, Tittel W and Zbinden H 2002 *Review on Modern Physics* **74** 145
[68] Mari A, Farace A, Didier N, Giovannetti V and Fazio R 2013 *Phys. Rev. Lett.* **111** 103605
[69] Bemani F, Motazedifard A, Roknizadeh R, Naderi M H and Vitali D 2017 *Phys. Rev. A* **96** 023805
[70] Giovannetti V, Lloyd S and Maccone L 2006 *Phys. Rev. Lett.* **96** 010401
[71] Mal S, Pramanik T and Majumdar A S 2013 *Phys. Rev. A* **87** 012105
[72] Zheng X and Zhang G-F 2017 *Quantum Inf. Process.* **16** 167
[73] Reyes-García R, Cruz S A and Cabrera-Trujillo R 2024 *Phys. Rev. A* **110** 022814
[74] Kozima H 2006 The science of the cold fusion phenomenon *In Search of the Physics and Chemistry Behind Complex Experimental Data Sets* (Elsevier Science)
[75] Pera J and Boronat J 2023 *Am. J. Phys.* **91** 90
[76] Belloni M and Robinett R W 2008 *Am. J. Phys.* **76** 798
[77] Belloni M and Robinett R W 2014 *Phys. Rep.* **540** 25
[78] Crank J and Nicolson P 1947 *Math. Proc. Camb. Phil. Soc.* **43** 50–67
[79] Griffiths D and Schroeter D 2018 *Introduction to Quantum Mechanics* (Cambridge University Press)
[80] Anis F, Roudnev V, Cabrera-Trujillo R and Esry B D 2006 *Phys. Rev. A* **73** 043414
[81] Cabrera-Trujillo R, Jiménez-Mier J and Juárez A M 2011 *Femtosecond-Scale Optics* ed P A Andreev (InTech)
[82] Majerník V and Majerníková E 2002 *J. Phys. A: Math. Gen.* **35** 5751
[83] Tamura A and Tatsumi Y 2017 *Eur. J. Phys.* **38** 065402
[84] Kälbermann G 1999 *Phys. Rev. A* **60** 2573